# Chapter 7

Resonant Magnetic Scattering from EuTe

With the huge magnetic scattering strengths at the lanthanide-M_5 thresholds that led to the observed pronounced magnetic reflections from thin holmium metal films (cf. Fig. 6.5), it should be possible to push magnetic scattering experiments even further towards an investigation of magnetic properties of a single atomic layer close to its ordering temperature and perhaps even above. However, in particular in the paramagnetic phase, any magnetic signal becomes arbitrarily weak. The amount of charge scattering background, more precisely the corresponding noise, becomes the limiting parameter of such experiments. This limit was reached in the previous study on thin Ho metal films at a thickness of about 12 ML. The magnetic signal of thinner films became hardly visible in the raw data. Even for thicker samples, the background subtraction yields rather noisy data, with only the main magnetic reflection observable. While this still permits to determine quantities like the ordering temperature or the magnetic modulation vector, the study of short-range magnetic correlations or small changes at the surface is difficult. The experiments are further impeded by the fact that in order to examine the influence of a surface on the bulk layers one has to probe the reciprocal space direction perpendicular to the surface, where reflections are superimposed on the surface reflectivity. Consequently, the measurements usually suffer from a substantial background signal. There are a few ways to enhance the magnetic contrast of a diffraction signal that occurs in specular direction. One can induce surface roughness in order to suppress the reflectivity, which has helped in the case of the polycrystalline holmium films, or one can study samples with a small miscut between the surface and the crystallographic rod, as done in the experiment on Y/Ho/Y structures [54]. However, such modifications might influence the magnetic properties. The solution chosen in the present work is different, as the studied compound EuTe intrinsically prevents the aforementioned limitations and furthermore combines all the necessary requirements of such a study, which is discussed in detail in the following sections.

7.1 Overview and Characterization

Like many other materials, e.g. NiO, the magnetic semiconductor EuTe crystallizes in the rock-salt structure as displayed in Fig. 7.1(a). The pure spin magnetism due to strongly localized electrons makes EuTe an almost ideal realization of the Heisenberg model. Therefore, EuTe was studied intensely as bulk material and in form of thin layers in superlattice structures [75,89]. The simple AFM structure[1] along the [111] direction ensures an ideal separation of charge and magnetic reflections as visualized in Fig. 7.1(b). Since the magnetic period length is twice the Eu monolayer distance, the magnetic reflection (blue) appears exactly half-way between the chemical Bragg peaks (black).


[1]See chapter 2.2 for a detailed discussion.
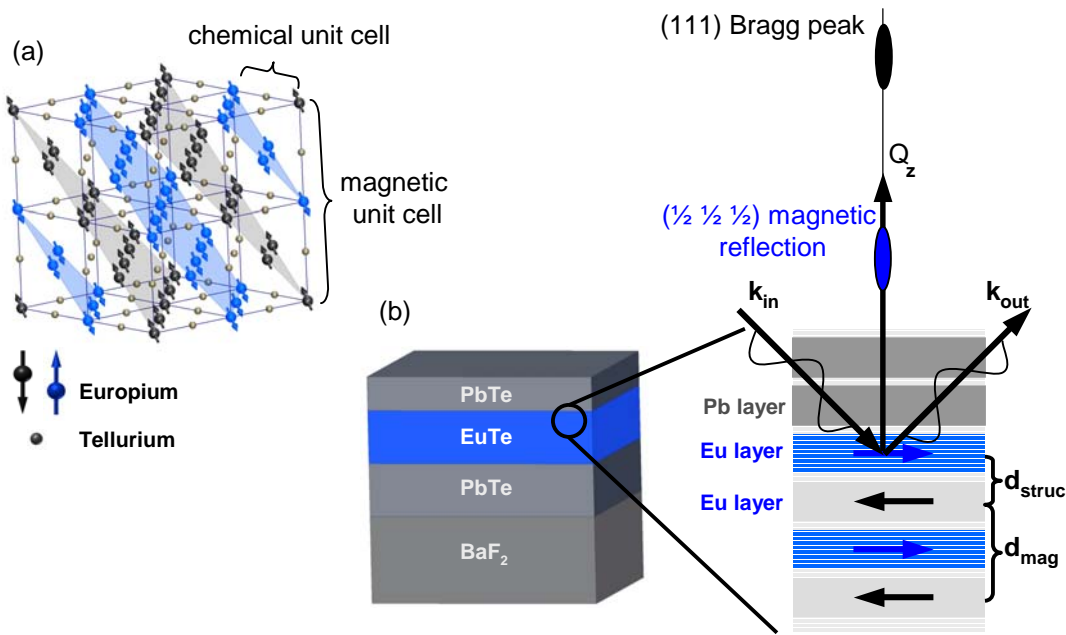
Figure 7.1: *(a) Magnetic unit cell of EuTe. The black and blue spheres represent Eu ions of different magnetization directions, while the smaller gray spheres represent the tellurium places. The AFM typeII structure of the Eu^{2+} fcc sublattice is characterized by ferromagnetically ordered (111) planes (black and blue planes) with alternating magnetization along the [111] direction. (b) Sample structure with EuTe(111) layers embedded between two PbTe films. The magnetic signal occurs along the specular direction.*

A $\Theta/2\Theta$-scan probes the EuTe [111] direction, i.e. the direction of the AFM modulation. The first chemical reflection along this direction, the (111) Bragg peak, is not accessible at the Eu-M_5 threshold at $h\nu = 1128$ eV. The (1/2,1/2,1/2) magnetic Bragg peak, however, is accessible at resonance. Figure 7.2 displays the observed magnetic diffraction signals from films of various thickness that demonstrate the advantage of EuTe for the present study, namely an ideal combination of lattice constant and energy position of the Eu-M_5 absorption threshold. The magnetic reflection at resonance appears very close to the Brewster angle ($2\Theta \approx 90°$). In the case of the here employed π-polarized incident light, this leads to an essentially perfect suppression of the charge-background signal at the position of the magnetic reflection and thus to magnetic diffraction signals of unprecedented quality and detailedness. These magnetic Bragg peaks are described by the Laue function, characterized by a principal maximum, whose position corresponds to the magnetic period length as well as several side maxima and minima at distances that quantify the number of contributing magnetic layers. For the thickest sample, the side maxima are directly visible in the raw data up to the seventh order. With decreasing sample thickness, the magnetic reflections broaden and the distance of the side minima increases, as expected. The huge magnetic contrast permits measurements down to only 2 ML of EuTe - the thinnest possible AFM system. As seen in Fig. 7.2, the studied EuTe(111) films allow to record magnetic Bragg reflections virtually free of background, which gives access to extremely weak magnetic order and allows to study the magnetic structure of these thin films in detail. This includes magnetic depth profiles, for the first time with atomic-layer resolution across an entire film, and the observation of short-range magnetic correlations above T_N down to correlation lengths of the order of the ionic distances.

The detailed quantitative analysis requires knowledge of structural and optical properties. This
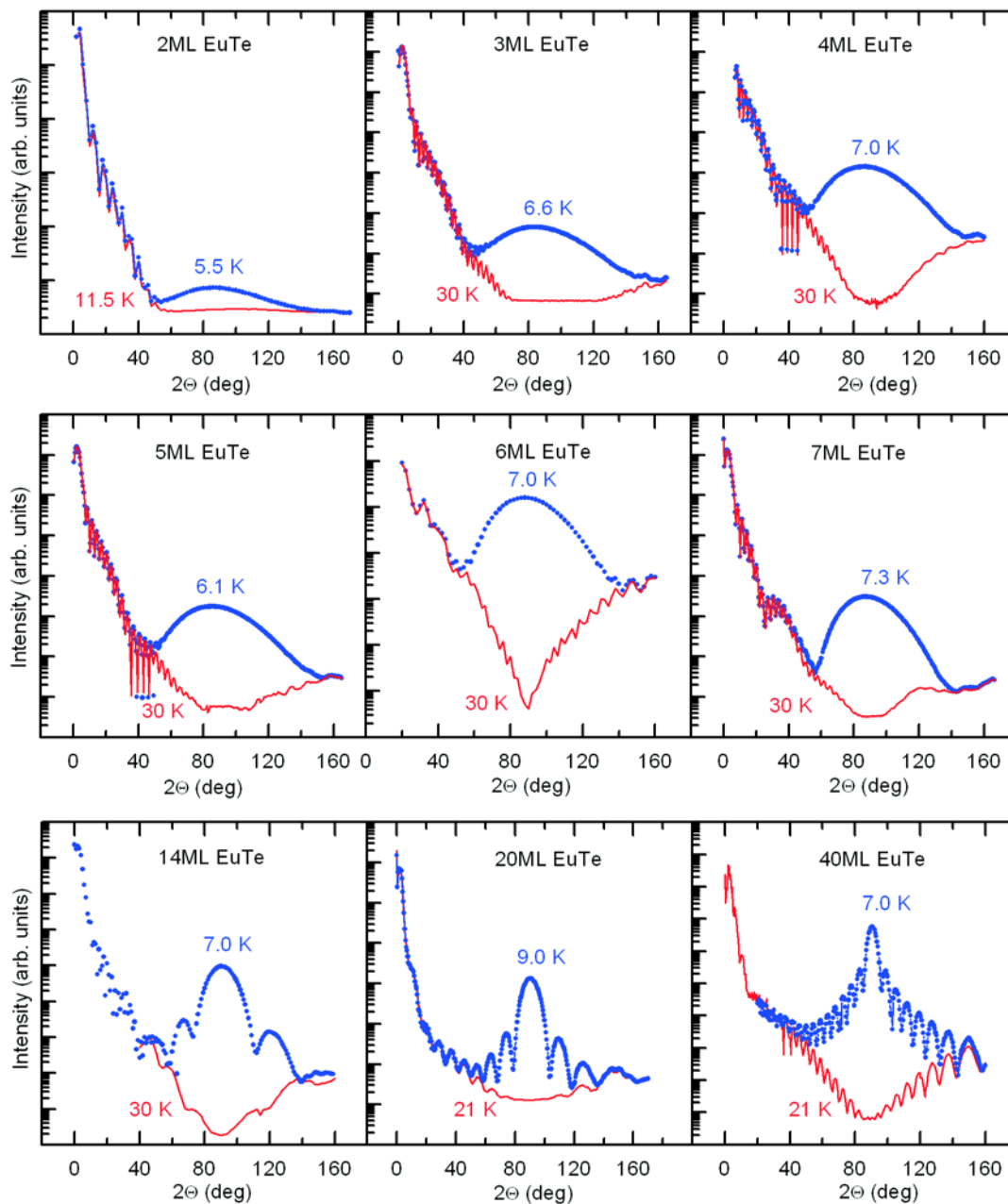
Figure 7.2: *Magnetic Laue patterns (blue) obtained by longitudinal scans from the EuTe samples. The red lines display the persisting charge reflectivity well above T_N.*
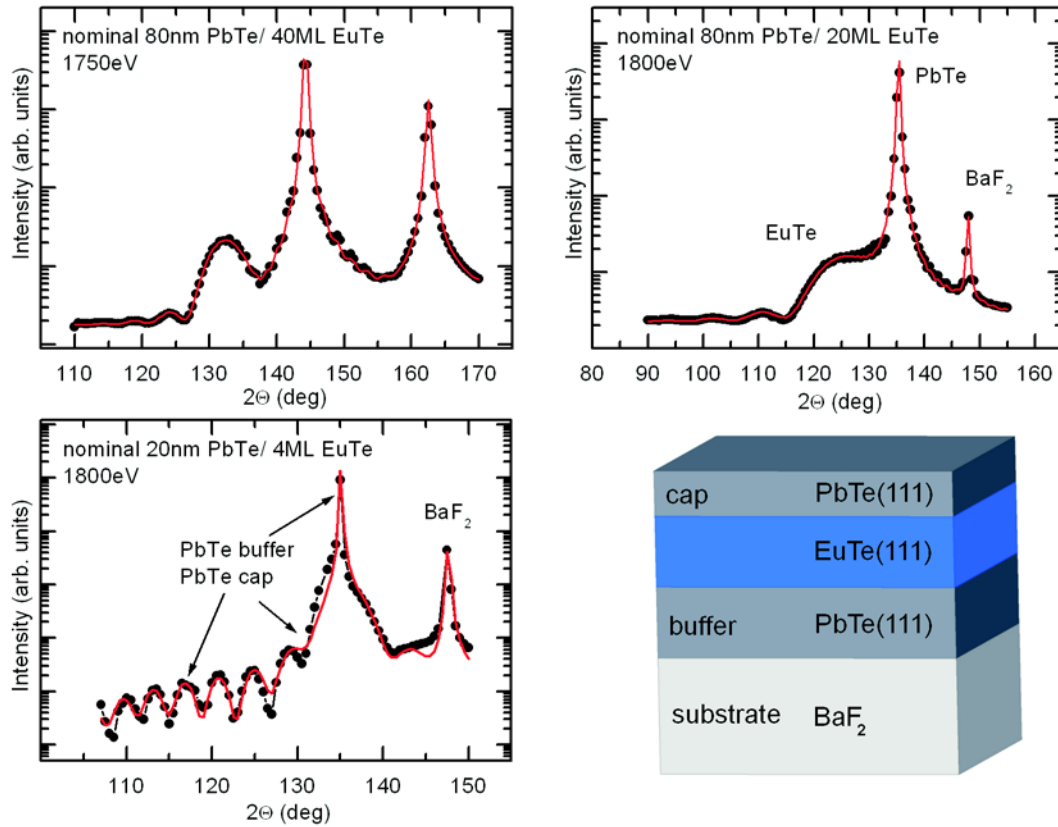
Figure 7.3: *Structural Bragg peaks of the nominal 40-ML (left,top), 4-ML (left, bottom) and the 20-ML EuTe sample (right, top). The red lines represent fits as described in the text. The given PbTe thicknesses refer to the nominal cap layer thicknesses. Bottom right: Sandwich structure of the studied samples.*

information can be extracted directly from the performed experiments, which will be the subject of the following sections. First, the macroscopic and crystalline properties of the EuTe films will be characterized, revealing the high structural quality of the studied samples. Thereafter, the energy-dependent properties, in particular the optical parameters at resonance, are discussed, which will enable us to estimate the magnetic scattering strength at the Eu-M_5 threshold. Subsequently, the polarization dependence of the magnetic signal is exploited to determine details of the macroscopic and microscopic magnetic structures of these films. This study will yield the polarization factor, necessary for a proper quantitative description of the measured Laue patterns. Finally, we shall address the quality of the magnetic structure in terms of domain size and coherence lengths and compare the findings with the crystalline properties.

7.1.1   Structural Properties

The samples studied in this thesis are single-crystalline EuTe(111) layers of various thicknesses. They were prepared in the group of Prof. Springholz at the University of Linz by means of molecular beam epitaxy (MBE), as discussed in detail in chapter 5.2. Each sample consists of a single thin EuTe(111) film embedded between two PbTe(111) layers on a BaF$_2$ substrate as displayed in Fig. 7.3, leading to essentially symmetric boundaries on both sides of EuTe. Several studies of EuTe epilayers and EuTe/PbTe superlattices (SL) had proven that these EuTe(111) samples are of very high crystalline

quality on a macroscopic scale with an interfacial roughness below one monolayer[2].

The present diffraction setup allows to characterize the structural properties together with the magnetism. Therefore, the structural properties are measured exactly at the same sample position as the magnetic signals. Two different measurements provide information on the structural properties: the chemical (111) Bragg peaks and the low-angle reflectivities.

The (111) Bragg reflection cannot be accessed at the Eu-M_5 resonance. Higher photon energies are needed, which is a typical limitation in soft x-ray diffraction with the flux characteristics of typical undulator beamlines. While the highly-developed undulators at BESSY II provide tremendous flux (up to 10^{14} photons per second) below 1 keV, free choice of polarization, and high energy resolution, the flux strongly decreases above 1 keV, which usually prevents experiments at photon energies of about 2 keV, typically necessary for the observation of chemical reflections. At such energies, it was exclusively the UE46-PGM beamline that provided the high photon flux required to obtain analyzable chemical reflections from these thin films. Figure 7.3 displays the diffraction curves obtained from nominal 4-ML, 20-ML and 40-ML samples, respectively, recorded at about 1.8 keV. The comparable size of the lattice constants of all ingredients of the sample, necessary for epitaxial growth, impedes the analysis: All chemical reflections occur at essentially the same positions in reciprocal space. The two dominating features belong to the BaF_2 substrate and the thick PbTe buffer layer, respectively. At smaller angles, a much broader Laue pattern originating from the EuTe film can be seen for the two thicker EuTe films. These Laue patterns are perturbed by the PbTe reflections at higher angles, but are well resolved on the low-angle side, which permits a determination of the EuTe thickness and the lattice constant with high accuracy. For the nominal 4-ML-thick EuTe sample only a structureless background is observed. Therefore, a precise evaluation of the EuTe thickness is not possible in the latter case. The pronounced oscillations, visible at smaller angles, belong to the Laue pattern from the thin PbTe cap layer of this sample. Also the PbTe scattering feature obtained from the nominal 20-ML and 40-ML sample cannot be described by a single line, but is a superposition of two reflections: a narrow intense one originating from the PbTe buffer and a broad component from the PbTe cap layer, both with essentially the same lattice constants.

The data can be readily described by Lorentzian lines for the PbTe buffer layer and the substrate crystal, as well as Laue patterns for the EuTe film and the PbTe cap layer, each of the form:

$$I(Q) \propto P(2\Theta) \left| f(Q) \left(\sum_{j=0}^{N-1} e^{-\frac{\mu j d}{\sin \omega}} e^{iQjd} + u e^{-\frac{\mu N d}{\sin \omega}} e^{iQjd} \right) \right|^2 \quad , \tag{7.1}$$

where d denotes the monolayer distance, N the number of layers, and P the polarization dependence. The absorption coefficient μ was taken from Ref. [99]. The parameter $0 \leq u \leq 1$ allows for possibly unfilled layers. The complex quantity f takes the different scattering contributions originating from the Eu/Pb ions and the Te ions into account:

$$f_x = f_{cation,x} + e^{iQ\frac{d_x}{2}} f_{Te} \text{ with x = Eu, Pb} \quad , \tag{7.2}$$

where the complex atomic scattering factors f_{Pb}, f_{Eu} and f_{Te} are taken from Ref. [99]. The data description uses equal lattice constants for the PbTe cap and the buffer films and the lattice parameter of the substrate crystal was fixed to the literature value of $d_{BaF_2} = 3.57$ Å [136], yielding the exact value of the photon energy.

The resulting structural parameters are summarized in table 7.1. The PbTe monolayer distance of (3.72 ± 0.01) Å agrees with the literature[3] value (3.73 Å) within rather small error bars. For the

---

[2]See chapter 5.2 for a detailed discussion.
[3]see chapter 5.2.1
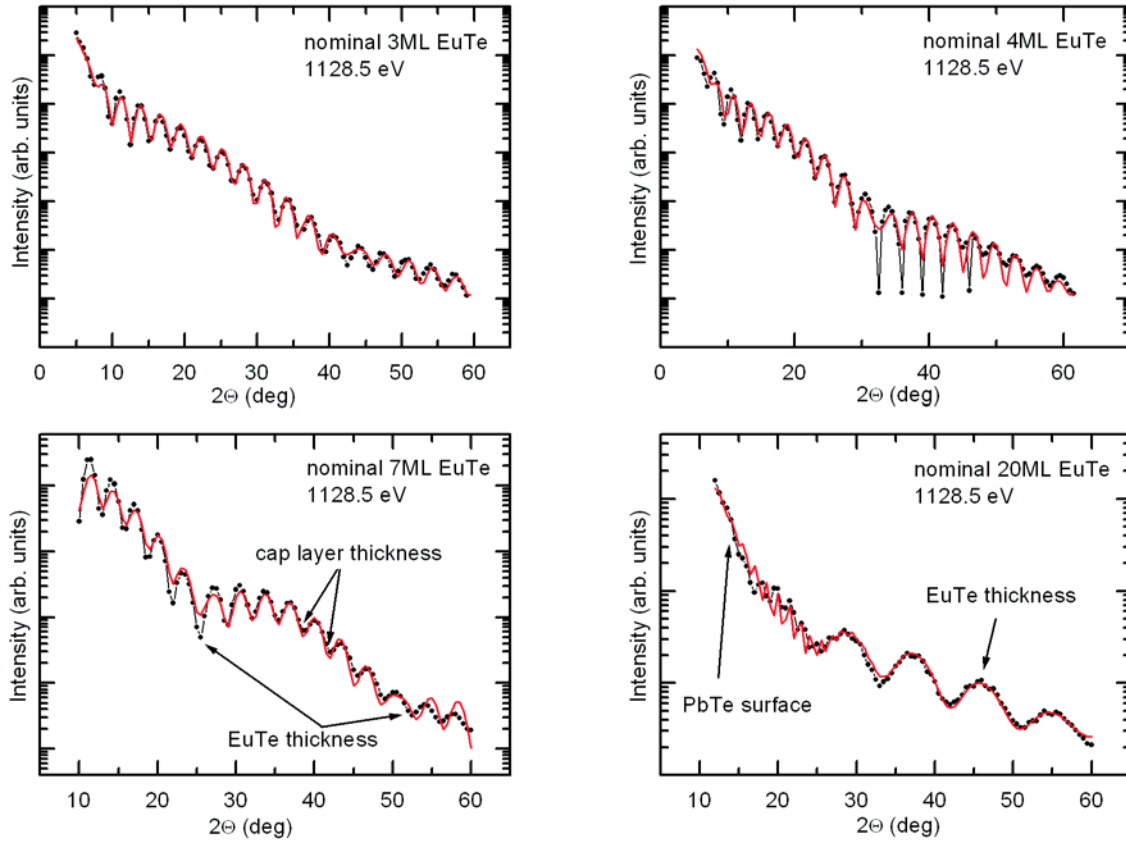
Figure 7.4: *Low-angle reflectivities recorded in the paramagnetic phase of EuTe. The red lines correspond to the fits according to the equations discussed in chapter 3.2.*

nominally 4-ML-thick sample, the cap layer thickness of (205 ± 10) Å is in excellent agreement with the nominal value of 200 Å. The EuTe thickness of this thin film can only be estimated to be smaller than 6 ML according to the associated broad diffraction feature. However, the results for the two thicker films are more precise. The EuTe thicknesses of (19.2 ± 1) ML and (43.6 ± 2) ML are consistent with the nominal values of 20 ML and 40 ML, respectively. However, it indicates a slightly larger coherent crystalline structure of the thickest EuTe sample. The EuTe monolayer spacing of (3.875 ± 0.02) Å agrees well with values reported in literature of 3.86 Å for superlattice samples containing thin EuTe layers [129]. This enhanced monolayer spacing with respect to the EuTe bulk value of 3.81 Å is due to an epitaxial strain of about 2%.

These findings can be compared with those obtained from the low-angle reflectivities in the paramagnetic phase. The rather small contrast between EuTe and PbTe leads to a structureless reflectivity at off-resonance energies. Only at the Eu-M_5 threshold, the different contributions can be clearly distinguished due to the resonant enhancement of the Eu scattering contribution. At small angles, the reflectivities are dominated by the contribution of the cap layer surface due to the negligible signal reflected from the interfaces as a consequence of photon absorption in the cap layer. It is followed by a region dominated by the interference of the photons scattered from the PbTe surface and the upper PbTe/EuTe interface, which causes rapid oscillations in the case of thick cap layers. At larger angles, the interference of photons scattered from both EuTe/PbTe interfaces superimposes much broader Kiessig fringes. The data description takes the contributions from the surface and the two interfaces,

nominal		reflectivity			(111) Bragg		
EuTe (ML)	cap (Å)	EuTe (ML)	cap (Å)	σ_{EuTe} (Å)	EuTe (ML)	cap (Å)	d_{EuTe} (Å)
3	200	3.9 ± 0.6	208 ± 10	4.5 ± 1.0			
4	200	5.4 ± 0.7	210 ± 10	4.0 ± 2.0	4.0 ± 2.0	205 ± 10	
5	200	4.9 ± 0.6	192 ± 10	4.5 ± 1.0			
7	200	6.7 ± 0.6	194 ± 10	3.0 ± 1.5			
20	800	19.9 ± 1.5	790 ± 40	3.0 ± 1.5	19.2 ± 1.0	840 ± 90	3.875 ± 0.020
40	800	43.8 ± 1.0	800 ± 50	3.5 ± 1.0	43.6 ± 2.0	730 ± 100	3.876 ± 0.020

Table 7.1: *Structural parameters of the studied EuTe films.*

calculated according to Eq. 3.19, into account. An additional damping term $e^{-0.5Q^2\sigma^2}$ accounts for the roughness, which was assumed to be equal for both interfaces. The total amplitude reflectivity was calculated recursively according to Eq. 3.21, which takes multiple reflection of the waves between the three boundaries into account. The total intensity reflectivity is given by the absolute square of this amplitude times the polarization dependence of incident π-polarized light. This leads to an excellent description of the data as shown in Fig. 7.4. The results are summarized in table 7.1. In all cases, the cap layer thicknesses agrees with the nominal values, given by the evaporation times during the sample preparation. The mean roughness of all EuTe/PbTe interfaces is found to be about one monolayer, in excellent agreement with RHEED and STM studies on comparable EuTe films (see chapter 5.2.1). The total EuTe thicknesses, obtained from these reflectivities, reproduce the results from the analysis of the (111) Bragg reflections, which are only sensitive to the coherent crystalline structure. Hence, the results clearly demonstrate a high crystalline quality of the entire EuTe films.

7.1.2 The Eu-M$_5$ Absorption Threshold

As in the experiments on the thin Ho metal films, it is the huge resonant enhancement of the magnetic scattering cross section at the lanthanide-M$_5$ absorption thresholds that provides the observed enormous magnetic contrast. This huge enhancement is theoretically well understood by the work of Hannon et al. [114], who predicted a magnetic scattering cross section at the lanthanide-M$_{4,5}$ resonances of the order of $100 r_0$. Experimentally, these predictions have been confirmed in a qualitative way and recently also quantitative studies. Ott et al. reported $240 r_0$ for the Ho-M$_5$ threshold [137]. Peters et al. obtained a similar result $\approx 200 r_0$ for the Gd-M$_5$ threshold [115]. Due to the same $4f$-electronic structure of the Eu^{2+} ($[Xe]4f^7$) and Gd^{3+} ($[Xe]4f^7$) ions, one expects similar resonance behaviors. The increase of the scattering strength at resonance is accompanied by significant energy-dependent changes of the index of refraction, $n = 1 - \delta + i\beta$, which has to be included into a quantitative data description. The rather thick PbTe cap layers of the EuTe samples inhibit a measurement of the absorption cross section by means of drain current/ total-electron-yield or fluorescence-yield methods. Nevertheless, the energy-dependent optical parameters can be quantified with sufficient accuracy from two independent measurements, the low-angle reflectivities in the paramagnetic phase and the energy-dependent behavior of the magnetic Bragg reflections. Reflectivities were discussed in detail in the previous section. The description of these reflectivities included δ and β as fit parameters. At the resonance maximum, one obtains $\delta = (2 \pm 2) \cdot 10^{-3}$ and $\beta = (3.0 \pm 1.5) \cdot 10^{-3}$, similar values as reported for holmium metal [54]. However, the atomic density of Eu in the EuTe samples is reduced by a factor of about two compared to metallic holmium, which indicates a larger scattering strength of
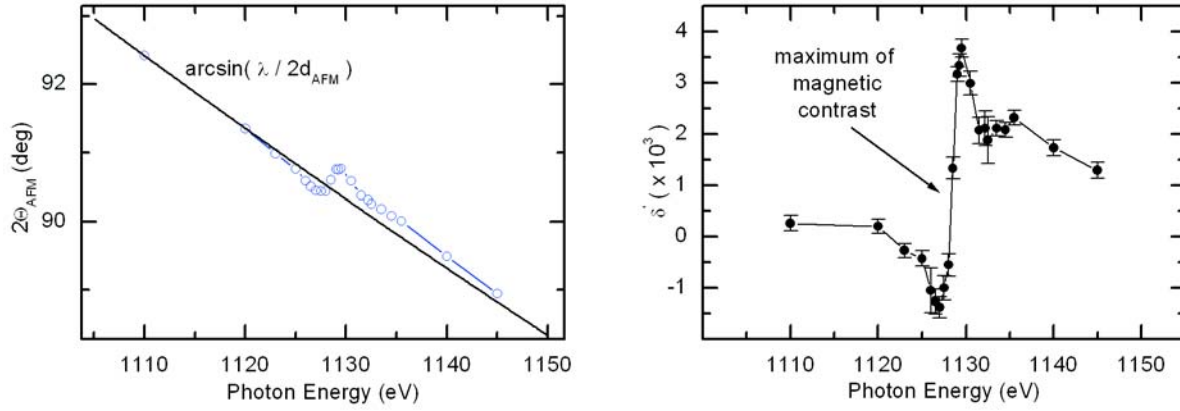
Figure 7.5: *Left: Energy-dependent position of the AFM Bragg peak of the 40-ML EuTe sample (blue dots). The pure arcsine behavior according to Bragg's law (solid line) is shown for comparison. Right: Corresponding optical parameter δ' that describes the displacement of the AFM peak in terms of a real index of refraction.*
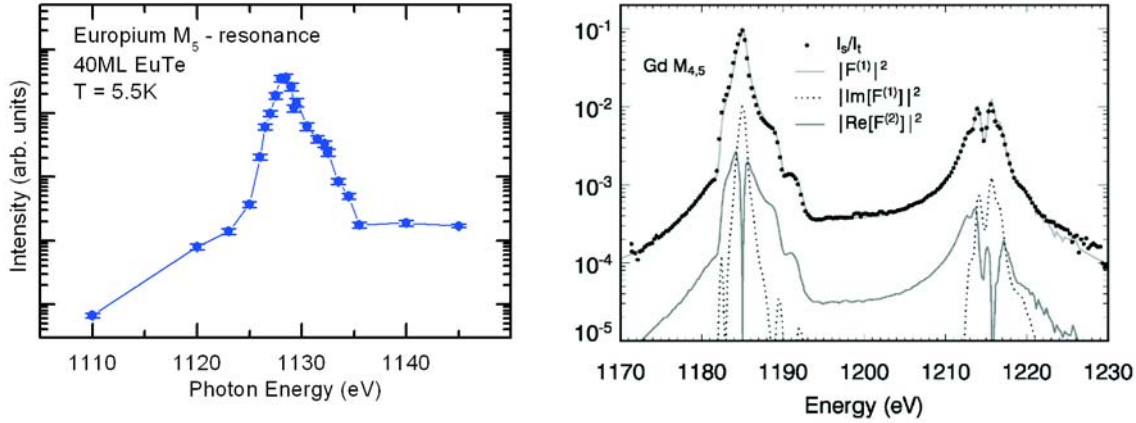
Figure 7.6: *Left: Energy-dependent integrated intensity of the magnetic Bragg peak of the 40-ML EuTe sample across the Eu-M_5 resonance. Right: Resonant scattering strength obtained from Gd^{3+} at the Gd-$M_{4,5}$ threshold (from Ref. [115]).*

the Eu ions. With Eqs. 3.14 and 3.17, the real and imaginary part of the atomic scattering length of the europium ions can be calculated. With the atomic density of Eu in EuTe one obtains $|Re(f)| = 350$ and $|Im(f)| = 530$, which agrees with the values obtained for gadolinium, as expected from the identical $4f$-electronic structures.

The energy dependence of the magnetic reflections contains three pieces of information: The energy-dependent scattering factor by the magnetically scattered intensity, the real part of the index of refraction via the displacement of the magnetic reflection from the position given by Bragg's law, and the imaginary part from the broadening of the Laue patterns as a consequence of the reduced photon penetration depth at resonance. However, even in the case of the thickest EuTe sample studied, the longitudinal broadening was hardly visible, revealing that the penetration depth is significantly larger than the sample thickness of 40 ML. This renders an accurate determination of β difficult, but demonstrates on the other hand the weak influence on the measured intensity distribution.

In contrast to β, the real part of n can be obtained with high accuracy from the energy-dependent

displacement of the magnetic Bragg reflections from the position according to Bragg's law, as depicted in Fig. 7.5. The black line corresponds to the pure arcsine behavior expected for an index of refraction of $n = 1$. Neglecting the weak influence of β, a quantity $\delta' \approx \delta$ can be calculated from the displacement of the magnetic peak position [138] in terms of a real index of refraction $n = 1 - \delta'$, only. According to Eq. 3.18, n reads:

$$n = 1 - \delta' = \frac{\cos \Theta_{AFM}}{\cos \left(\arcsin \frac{\lambda}{2d_{AFM}} \right)} \quad , \tag{7.3}$$

where Θ_{AFM} denotes the observed angle of incidence for the magnetic reflection, d_{AFM} the magnetic period length, and λ the wavelength of the photons. The resulting δ' values are given in the right panel of Fig. 7.5. They fairly agree with the results from the low-angle reflectivities, but have a much higher quality. They show, in particular, that corrections for refraction effects are negligible at the energy position of maximum magnetic contrast. Without attempting an accurate determination of the resonant magnetic scattering strength, an estimate is given here, in order to check the validity of the kinematical approximation used in the following analysis. The observed magnetic Laue patterns originate from the circular dichroic part of the resonant scattering amplitude, i.e. F^1 (see Eq. 3.38). Figure 7.6 displays the energy-dependent integrated magnetic intensity across the M_5 resonance of Eu, again demonstrating the enormous enhancement of the magnetically scattered intensity at this threshold. At the maximum of the resonant enhancement, the observed peak intensity corresponds to more than $1 \cdot 10^{-4}$ of the incident intensity I_0. This value, however, underestimates the magnetic scattering strength, since additional influences like absorption in the cap layer or the polarization factor have to be taken into account, as discussed in detail in appendix A. According to Eq. 3.22, replacing the electronic density by the atomic density of the europium ions times their magnetic atomic scattering strength F^1, the magnetic amplitude reflectivity per layer g is given by:

$$|g| = \frac{\lambda r_0}{A \sin \Theta_{AFM}} |F^1| \quad , \tag{7.4}$$

where A denotes the two-dimensional unit-cell area in the hexagonal planes. With Eq. 7.4, the normalized peak intensity is $I_0 N^2 m^2 g^2$, with N being the number of magnetic layers and m the order parameter.

The resulting $|F^1|$, obtained from all samples are summarized in table 7.2, giving a consistent value $|F^1| \approx 150 \, r_0$ for all samples. These numbers are somewhat smaller than those reported for

N	$|F^1|$
(ML)	(r_0)
3	130
4	150
5	140
7	150
14	150
20	150
40	130

Table 7.2: *Resonant magnetic scattering strength $|F^1|$ at the Eu-M_5 threshold, calculated from the magnetically scattered intensities for samples of different thicknesses.*

gadolinium. However, the peaks were measured with an energy resolution of about 0.9 eV, which causes an averaging over a substantial part of the magnetic resonance. Therefore, the present values correspond to approximately 75% of the maximum scattering strength, which indicates a maximum value of $|F^1| \approx 200r_0$, in excellent agreement with the value reported previously for Gd. This corresponds to an amplitude reflectivity per Eu layer of $\approx 5 \cdot 10^{-3}$ and points out a very important fact, crucial for the subsequent data analysis: According to the discussion of the dynamical scattering theory (chapter 3.4), all samples can be described within the kinematical approximation!

7.1.3 Polarization Dependence: The Magnetic Structure

With these more technical, albeit important, aspects we now turn to the main subject - the study of the magnetic properties of EuTe. The first question addresses the microscopic and macroscopic magnetic structure of the samples, i.e. the type and distribution of domains in the sample. From this we will obtain information on the last unknown geometry-dependence, the polarization factor of the magnetic scattering, which is essential for a precise quantitative analysis of the magnetic patterns. Unlike the polarization dependence in charge scattering, which depends only on the polarization of the incident light and the scattering angle, the resonant magnetic scattering process involves changes of the polarization with an angular dependence determined by the local magnetization direction. In the present experiment, the magnetic signals result from the circular dichroic resonant magnetic scattering contribution (see Eq. 3.38), and the corresponding polarization factor $(\hat{\epsilon}_f^* \times \epsilon_i)\mathbf{m}$ has to be worked out. With $\mathbf{m} = (m_x, m_y, m_z)$, $|\mathbf{m}| = 1$, where m_x, m_y, m_z refer to the vertical, horizontal and perpendicular magnetization components with respect to the scattering plane and sample surface, respectively, the corresponding polarization factors for the scattering channels in horizontal specular scattering geometry are the following (see Eq. 3.38):

$$
\begin{aligned}
P_A(\mathbf{m}, \Theta)_{\pi \to \pi} &= -m_x \sin 2\Theta \\
P_A(\mathbf{m}, \Theta)_{\pi \to \sigma} &= m_z \sin \Theta + m_y \cos \Theta \\
P_A(\mathbf{m}, \Theta)_{\sigma \to \pi} &= m_z \sin \Theta - m_y \cos \Theta \quad .
\end{aligned}
$$

Non-resonant and resonant charge scattering are described by:

$$
\begin{aligned}
P_A(\mathbf{m}, \Theta)_{\pi \to \pi} &= \cos 2\Theta \\
P_A(\mathbf{m}, \Theta)_{\sigma \to \sigma} &= 1 \quad .
\end{aligned}
$$

The subscript A indicates that these factors refer to the scattered amplitudes. As can be seen, the magnetic $\pi \to \pi$ scattering approaches a maximum at $2\Theta = 90°$, while charge scattering for π-polarized incident light is strongly suppressed at this angle. Therefore, π-polarized incident light yields the maximum magnetic contrast at the position of the EuTe magnetic Bragg peak, as demonstrated in Fig. 7.7. However, the various scattering contributions can give rise to complicated interference effects. A precise data analysis requires therefore a knowledge of the magnetization directions and their distribution within the sample. This information is included in the polarization dependence of the measured magnetic signals. However, the overall magnetic structure cannot be clarified by the present experiment, since this would require to probe different magnetic reflections, which are not accessible within the limited reciprocal space of soft x-ray experiments. This is one of the reasons, why magnetic neutron scattering is still the method of choice to determine magnetic structures.

The magnetic structure of thin EuTe epitaxial layers is well known from several magnetic neutron studies on superlattices (SL) [75, 89]. These studies revealed bulk-like simple AFM structures, even
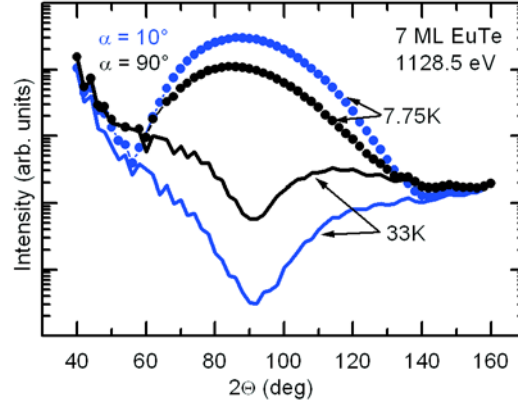
Figure 7.7: *Longitudinal scans above (solid lines) and below the ordering temperature (dots) of the 7-ML EuTe sample for nearly π-polarized (blue) and σ-polarized (black) incident light.*

in the case of EuTe layers as thin as 2 ML. While bulk EuTe is characterized by four equivalent T-domains, in thin epitaxial layers only the T-domain with ferromagnetically ordered planes parallel to the surface persists. This experimental result is explained by the epitaxial strain causing a decrease of the nn distance parallel to the surface, which results in a significantly enhanced nn coupling of the ions within the planes parallel to the surface. In the present experiment, the pronounced magnetic reflections at the reciprocal (1/2,1/2,1/2) position clearly demonstrate the presence of the simple AFM structure perpendicular to the surface.

The most important question regarding the subsequent analysis of the Laue patterns concerns the distribution of possible S-domains, i.e. the orientation of the magnetic moments of the FM planes with respect to the crystallographic axes. The above-mentioned magnetic neutron diffraction experiments suggest that all six possible S-domains are equally populated. This can be clarified in the present experiment by measuring the 2Θ dependence of the magnetically scattered intensity for systematically varied angle of the linear polarization of the incident light, as well as for different azimuthal orientations of the sample surface. Any linearly polarized incident beam can be separated into two perpendicular linear components:

$$\mathbf{E}(t) = \cos\alpha\epsilon_\pi E(t) + \sin\alpha\epsilon_\sigma E(t) \quad , \tag{7.5}$$

where α is the angle between $\mathbf{E}$ and the scattering plane. Hence, in general, the magnetically scattered amplitudes will contain contributions from both, the π and the σ channel, with a polarization dependence given by the sum of the two channels:

$$P_A(\alpha, \mathbf{m}, \Theta)_\pi = \cos\alpha\, P_A(\mathbf{m}, \Theta)_{\pi\to\pi} + \sin\alpha\, P_A(\mathbf{m}, \Theta)_{\sigma\to\pi} \tag{7.6}$$

$$P_A(\alpha, \mathbf{m}, \Theta)_\sigma = \cos\alpha\, P_A(\mathbf{m}, \Theta)_{\pi\to\sigma} \quad . \tag{7.7}$$

Hence, the magnetic intensity measured in the experiment is modulated according to:

$$P(\alpha, \mathbf{m}, \Theta) = P_A^2(\alpha, \mathbf{m}, \Theta)_\pi + P_A^2(\alpha, \mathbf{m}, \Theta)_\sigma \quad , \tag{7.8}$$

which leads to a sum of three terms, each containing the square of one of the magnetization components, and three interference terms containing the product of two of the components of $\mathbf{m}$. Examples of polarization-dependent intensities are given in Fig. 7.8. The top panel displays Laue patterns from
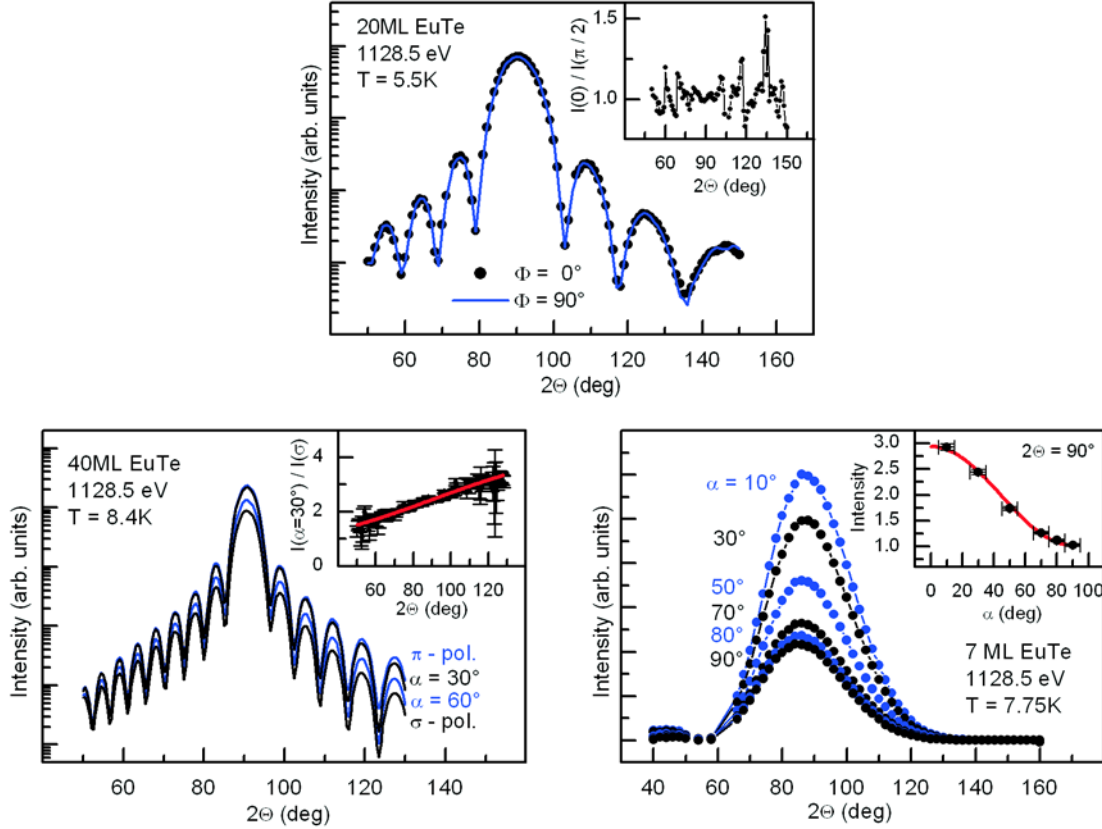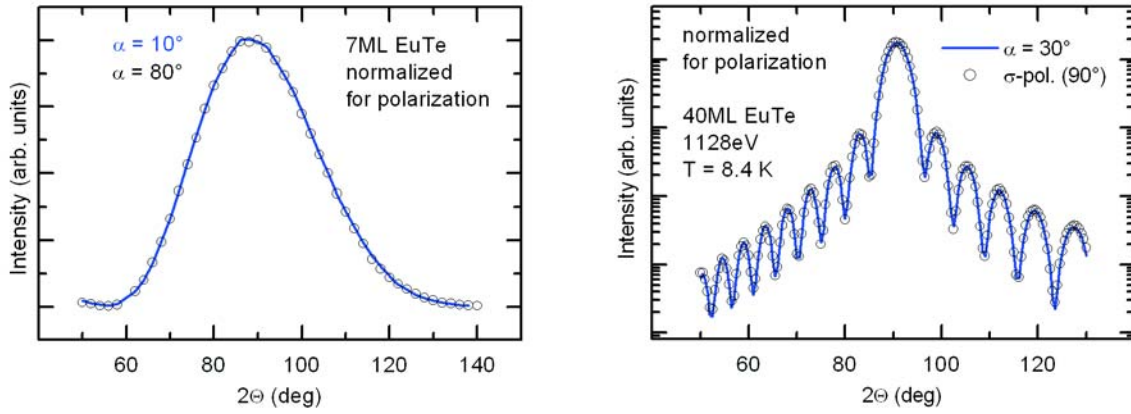
Figure 7.8: *Polarization dependence of the magnetic reflections. Top: Laue patterns from the 20-ML EuTe sample measured for $\Phi = 90°$ and $\Phi = 0°$. Bottom: Magnetic reflections from the 7-ML (right) and 40-ML (left) sample. Inset of the right panel: α dependence of the scattered intensity at $2\Theta = 90°$. Inset of the left panel: 2Θ dependence of the ratio $\frac{I(30°)}{I(90°)}$ of the two Laue patterns measured with $\alpha = 30°$ and $\alpha = 90°$ (σ light). The red lines are calculated (see text).*

the 20-ML sample obtained for two different azimuthal angles Φ. Both magnetic signals are essentially equal as can be seen from the ratio given in the inset. This ratio does not show any systematic deviation from one, as it would be the case, if m_x and m_y were different. The two lower panels show the magnetic peaks obtained from 7 ML and 40 ML of EuTe for different polarization directions of the incident linearly polarized light, where α denotes the angle between the scattering plane and the polarization direction, i.e. $\alpha = 0$ for π-light. The inset of the bottom right panel of Fig. 7.8 displays the peak intensities from 7 ML of EuTe at $2\Theta = 90°$ as a function of α, and the inset of the left panel shows the ratio of the Laue patterns of 40 ML EuTe measured for $\alpha = 30°$ and $\alpha = 90°$.

With the polarization factor (Eq. 7.8), these experimental results are readily reproduced, if all interference terms are neglected and $m_z^2 = 0$ and $m_x^2 = m_y^2$ is assumed (red lines in the insets of Fig. 7.8). This scenario corresponds to the absence of antiferromagnetically correlated spin components perpendicular to the surface and a cancellation of the two in-plane magnetization components on a macroscopic scale, i.e. an equal distribution of all six S-domains with the magnetization vectors confined to the hexagonal planes.

From this scenario, the polarization factors that describe the angular dependence of the scattered magnetic intensity for π and σ incident light in specular geometry read :

Figure 7.9: *Magnetic signals from the 7-ML and 40-ML sample, measured for nearly π-polarized incident light (blue) and nearly σ-polarized incident light (black), after correction for the polarization dependence.*

$$P_\pi \quad \propto \quad \sin^2 2\Theta + \cos^2 \Theta \qquad\qquad (7.9)$$
$$P_\sigma \quad \propto \quad \cos^2 \Theta \quad , \qquad\qquad (7.10)$$

where the subscript refers to the polarization of the incident light.

The validity of these polarization factors is demonstrated in Fig. 7.9. The displayed curves belong to magnetic signals measured for different polarizations of the incident light. After the proper normalization of the magnetic intensities using Eqs. 7.9 and 7.10, the patterns are identical. The absence of any difference in the normalized data for π-incident light from those of σ-light, even at 2Θ positions where the magnetic signal and charge scattering are of comparable magnitude, clearly reveals that no disturbing magnetic-charge interference has to be taken into account.

This section used the polarization dependence of resonant magnetic soft x-ray scattering to clarify the magnetic structure of the studied EuTe samples, the types of domains present as well as their macroscopic distribution. The resulting rather simple polarization dependence in the case of π-polarized incident light and the absence of disturbing magnetic-charge interference allows to apply π-polarized incident light in the following studies, making use of the high magnetic contrast provided by π-polarized light. All samples thicker than 2 ML exhibit the bulk-like simple AFM structure along the [111] direction normal to the surface, characterized by an equal distribution of domains with the possible in-plane magnetizations in agreement with the results from magnetic neutron diffraction on SL systems. The following section addresses the size of the magnetic domains.

7.1.4 In-Plane Coherence and Magnetic Thickness

With the knowledge of the optical parameters and the polarization dependence, a quantitative description of the measured longitudinal Laue patterns has now become possible. Such patterns provide two pieces of information: (i) Due to the simple AFM structure of EuTe, the positions of the magnetic reflections in reciprocal space determine the spacing of the corresponding Bragg planes. (ii) The width of the Laue pattern allows to quantify the number of contributing magnetic layers. In connection with the rocking scans, detailed information on the domain sizes is obtained.

We start the discussion with the in-plane coherence of the magnetic structure, which is given by the width of the rocking scans at the position of maximum magnetic intensity. In x-ray diffraction
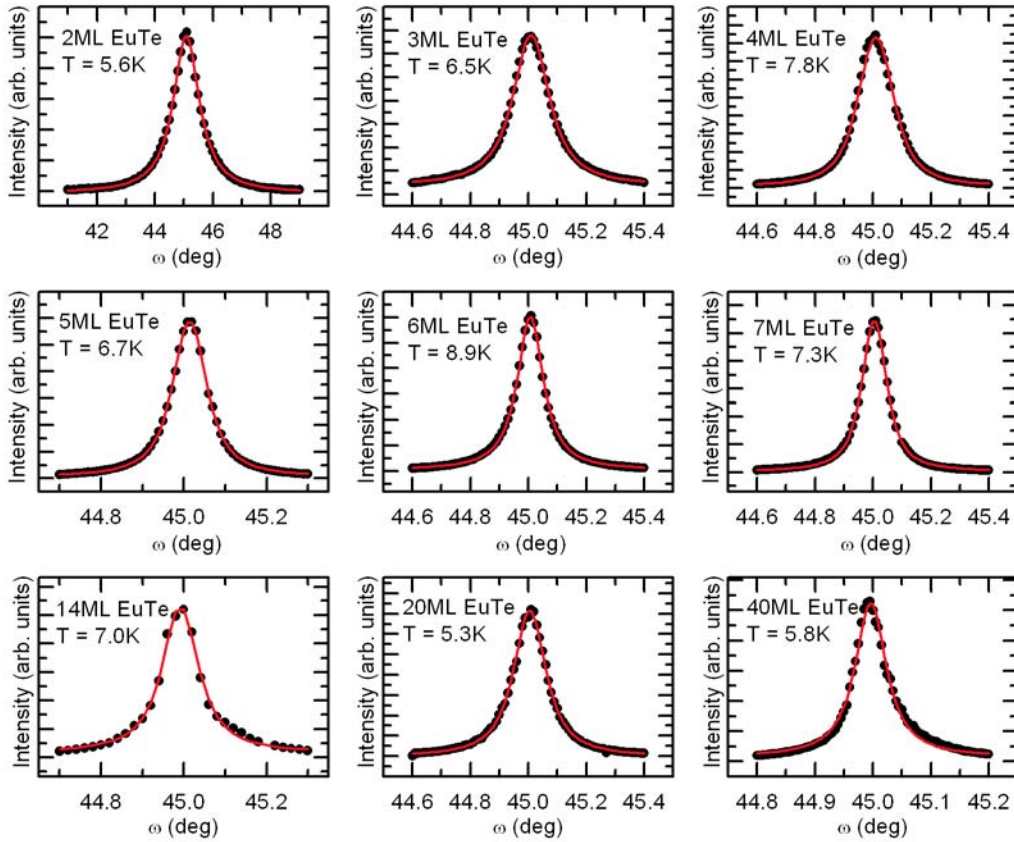
Figure 7.10: *Rocking scans performed at the maximum of magnetic intensity well below T_N. The measured data (dots) are readily described by Lorentzian lines (red curves) as discussed in the text.*

from thick samples, a rocking scan integrates over the mosaic blocks characterized by slightly tilted Bragg planes with respect to the macroscopic surface. In such a scenario, the Laue conditions for all three reciprocal space directions are sharp as a consequence of the typically large size of the mosaic blocks. Therefore, a rocking scan does not depend significantly on the angular acceptance of the detector and the expected line shape is a Gaussian. The situation is different in the present thin-film experiments. The magnetic peaks are significantly broadened in the Q_z direction. Therefore, the width and line shape of a transversal scan depend on the resolution function of the detector. Furthermore, the observed transversal line shape is not a Gaussian but a Lorentzian. This observation agrees with the findings of several other studies [139] and, as shown by Lee et al. [134], can be caused by a distribution of domains at the surface, if the signal is integrated along the vertical direction by a large detector acceptance[4] as in the present experiment. The HWHM of this Lorentzian is the inverse of the average domain size. Figure 7.10 displays the rocking scans from all samples well below T_N. The data are readily described by a Lorentzian line convoluted with the resolution function of the detector. From these fits, the lateral magnetic domain sizes were determined, summarized in Fig. 7.11. The size of $\approx$ 150 nm matches the structural limitation given by the growth spiral edges of a mean distance of 150 nm as discussed in chapter 5.2.1 and therefore indicates that the magnetic domains are limited by

---

[4]Lee derived a two-dimensional line shape. If this result is integrated along one reciprocal space direction a Lorentzian results.
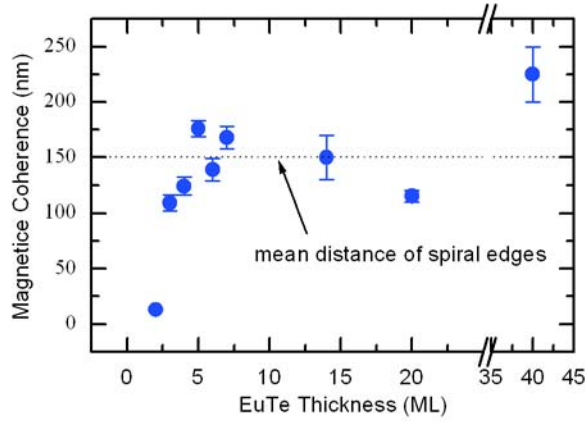
Figure 7.11: *Results for in-plane magnetic coherence.*

the structural imperfections. This is further supported by the significantly larger coherence length of the 40-ML sample, where the spiral structure on the surface should have vanished (see chapter 5.2.1). Only the 2-ML sample is characterized by a peak width one order of magnitude larger than observed for all other samples. For this sample, however, the width depends on temperature, which indicates that even at the lowest achieved temperature the phase transition is not completed and the increasing rocking width is due to short-range correlations. All other samples are characterized by a constant in-plane width within the ordered phase. This large magnetic coherence length clearly reveals the high in-plane magnetic quality of all samples, characterized by large coherent domains.

In contrast to this narrow transversal width, the longitudinal intensity distribution is broad as a consequence of the finite thickness of the EuTe films. According to appendix A, the measured longitudinal intensities $I(Q_z)$ are described by the finite one-dimensional lattice sum:

$$I(Q_z) \propto m^2 \left| \sum_{j=0}^{N-1} (-1)^j e^{-\frac{jd\mu}{\sin\Theta}} e^{iQ_z dj} \right|^2 \quad , \tag{7.11}$$

where N counts the number of contributing layers, m is the AFM order parameter, and d denotes the monolayer distance. The real exponential term considers the attenuation of the beam within the EuTe. A proper application of this formula to the measured intensities has to take further geometry dependences into account as derived in appendix A, namely the absorption of incident and scattered photons in the PbTe cap layer, the integration over the detector acceptance as well as the illuminated sample volume and the polarization factor.

In the following, the measured magnetic intensities are normalized with respect to these geometry-dependent influences, and the resulting pure Q_z dependence, where Q_z is calculated according to Eq. 3.39, is analyzed in terms of the simple one-dimensional lattice sum. Representative results of the normalization procedure are shown in Fig. 7.12. The normalized magnetic peaks are perfectly symmetric for all samples, as expected from the remaining lattice sum, which nicely demonstrates the validity of the derived geometry dependences. The principal maxima of the normalized data can be readily described by means of a Gaussian[5] multiplied by the AFM form factor $\left|1 - e^{iQ_z d}\right|^2$. This analysis neglects the side minima of the Laue patterns, but still provides an accurate value of the mean number of magnetic layers. From the peak positions, the monolayer spacing of all samples can be

---

[5]The Gaussian function is known to be a reasonable approximation of the main maximum of a Laue pattern.
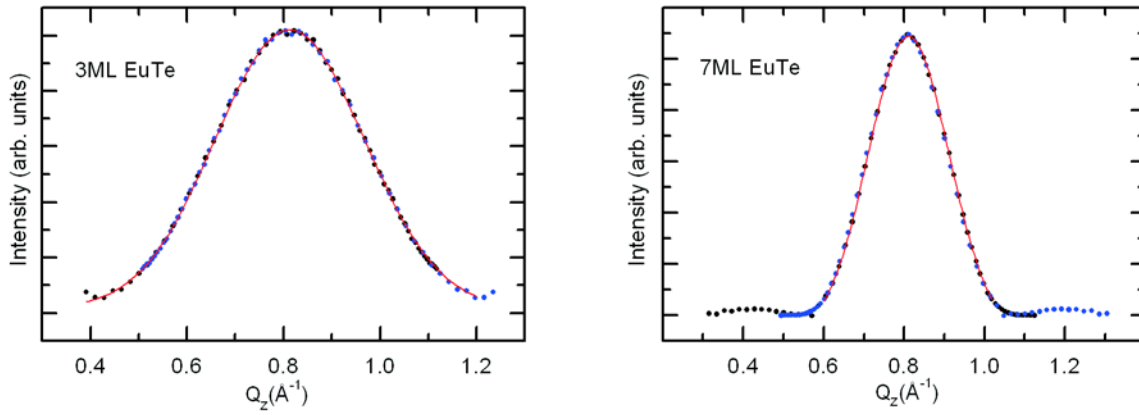
Figure 7.12: *Normalized magnetic signals of the 3-ML and 7-ML sample (black dots). The coincidence with the corresponding mirrored pattern (blue dots), obtained by mirroring the data at a vertical axis through the maximum of intensity, reflects the proper normalization procedure. The red curves represent Gaussian fits to the principal maxima as described in the text.*

determined due to the known AFM structure. Note, that this method provides the only possibility to determine the monolayer distance of such thin MBE films, because each chemical reflection would be fully dominated by the PbTe contributions, which prevents a precise determination of the lattice constant by non-resonant experiments. The obtained monolayer distances are shown in Fig. 7.13. The results for all EuTe samples are essentially equal within the error bars, as expected in the case of pseudomorphic growth of EuTe up to 45 ML of thickness.

The peak widths provide information on the EuTe film in terms of contributing magnetic layers. The results are summarized in table 7.3. The number of contributing magnetic layers essentially equals the chemical thickness. Hence, all samples are characterized by a high-quality crystalline structure, where all layers contribute to the magnetic structure, i.e. no magnetically dead layers exist.

The analysis discussed so far demonstrates the large amount of information that can be obtained from thin magnetic samples by means of resonant soft x-ray scattering. The accessible properties are not restricted to the magnetic behavior, but also structural and energy-dependent quantities could be determined, which led to a comprehensive characterization of various aspects of the studied samples
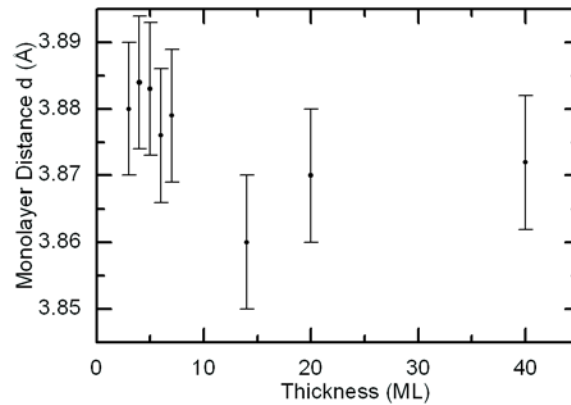
Figure 7.13: *Monolayer distance in the studied EuTe samples.*

thickness		
nominal (ML)	chemical (ML)	magnetic (ML)
3	3.9 ± 0.6	3.5 ± 0.2
4	5.4 ± 0.7	4.8 ± 0.3
5	4.9 ± 0.6	4.5 ± 0.3
6		5.9 ± 0.3
7	6.7 ± 0.6	6.3 ± 0.4
14		13.1 ± 1.5
20	19.9 ± 1.5	19.9 ± 1.0
40	43.8 ± 1.0	43.0 ± 2.0

Table 7.3: *Samples thicknesses obtained from the chemical (111) reflection and the magnetic superstructure satellites.*

by a single experiment. The results reveal the high magnetic and structural quality of all EuTe epilayers down to 3 ML. All observed properties are within the expectations and agree with other results reported in literature for SL systems. In the present experiment, these properties were determined for the first time for single thin EuTe films, which once more demonstrates the capabilities of resonant soft x-ray scattering applied to ultra-thin systems. So far only static properties were discussed. The most inspiring results of this study arise from temperature-dependent changes as discussed in the following.

7.2 The Ordered Phase: Layer-Resolved Magnetization

Laue patterns of thin films contain detailed information on the scattering contributions of the individual layers, beyond the mean number of layers given by the spacing of the side minima. In the present case, a magnetic Laue pattern includes information on the complete magnetization profile across the thin film, which can be reconstructed as long as the number of atomic layers is not so large that the influence of the surface layers on the Laue pattern becomes negligible. However, it is not sufficient to reconstruct the magnetization profile from a single Laue pattern, since the spatial variation of the magnetization might reflect the chemical profile only. The key is its evolution with temperature, since the chemical profile will not change with temperature, while the number of magnetic layers influenced by the surface is predicted to increase with increasing temperature (see chapter 1.3.2).

Let us first consider the possible Laue patterns schematically (Fig. 7.14). For an ideal 20-ML-thick film (blue profile), at $T = T_1$, the corresponding Laue pattern is given by the blue lines in Fig. 7.14. (i) Suppose that the magnetization within the entire sample decreases homogeneously with temperature. In this case, the relative scattering contribution of each layer does not change with temperature. Therefore, a magnetic Laue pattern recorded at $T_2 > T_1$ differs only by a factor of $\left| \frac{m(T_1)}{m(T_2)} \right|^2$, as shown by the red line in the left panel of Fig. 7.14 ($m(T)$ denotes the order parameter). (ii) A faster decrease of the magnetic scattering contribution of the layers at the center of the sample results in a smaller spacing between the first side maxima and the main reflection. In addition, it would lead to a shift of the intensity from the principal reflection to the flanks as depicted in the center part of Fig. 7.14. In the extreme case of paramagnetic inner layers (gray), only a simple oscillation remains. (iii) A complete loss of surface layers (gray profile in the right panel) causes a change of the period
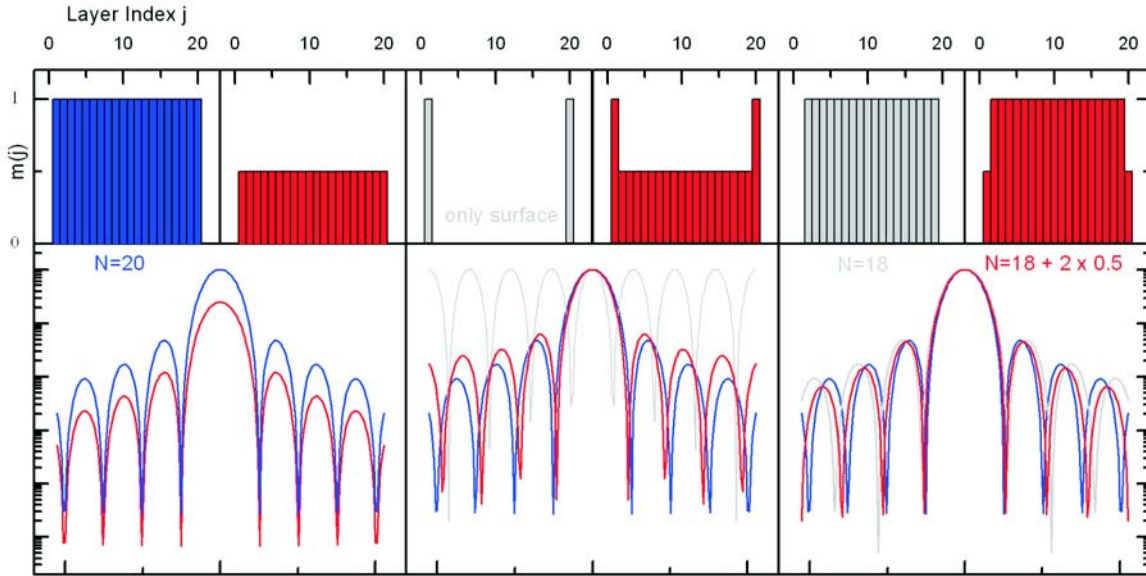
Figure 7.14: *Calculated Laue patterns for different real-space magnetization profiles.*

of the Laue oscillations, because the effective magnetic thickness of the film changes. The result is a broader Laue pattern with the side maxima and minima shifted away from the principal reflection, however, with an essentially unchanged ratio of peak heights of the principal maximum and the first side maximum[6]. In addition, a reduced but not vanishing contribution from the surface (red pattern) would have a similar effect as roughness on the reflectivity and would cause a faster decrease of the intensity on the flanks of the Laue pattern. This demonstrates the high sensitivity of a Laue pattern on details of the real-space structure.

Figure 7.15 displays the *observed* temperature behaviors of the magnetic Laue patterns for the 40-ML and 20-ML films. Evidently, the patterns do not only decrease in intensity with increasing temperature. The side maxima shift outwards with respect to the principal reflection when the temperature is raised. Furthermore, as inferred from the scaled patterns shown in the inset, the intensities of the side maxima decrease faster than those of the principal reflection. Therefore, one can conclude already from an inspection of the raw data, that scenario (iii) applies: a faster decrease of the scattering contribution from the sample surfaces with increasing temperature.

The following discussion of this experimental finding starts with a more qualitative discussion giving an overview on the behaviors of all films. Even without a detailed quantitative analysis, important aspects can be readily concluded just by straightforward inspection of the magnetic Laue patterns. For selected film thicknesses, a quantitative analysis was carried out, yielding atomic-layer-resolved magnetization profiles.

---

[6]This ratio is about $\frac{9}{4}\pi^2$, for large N.
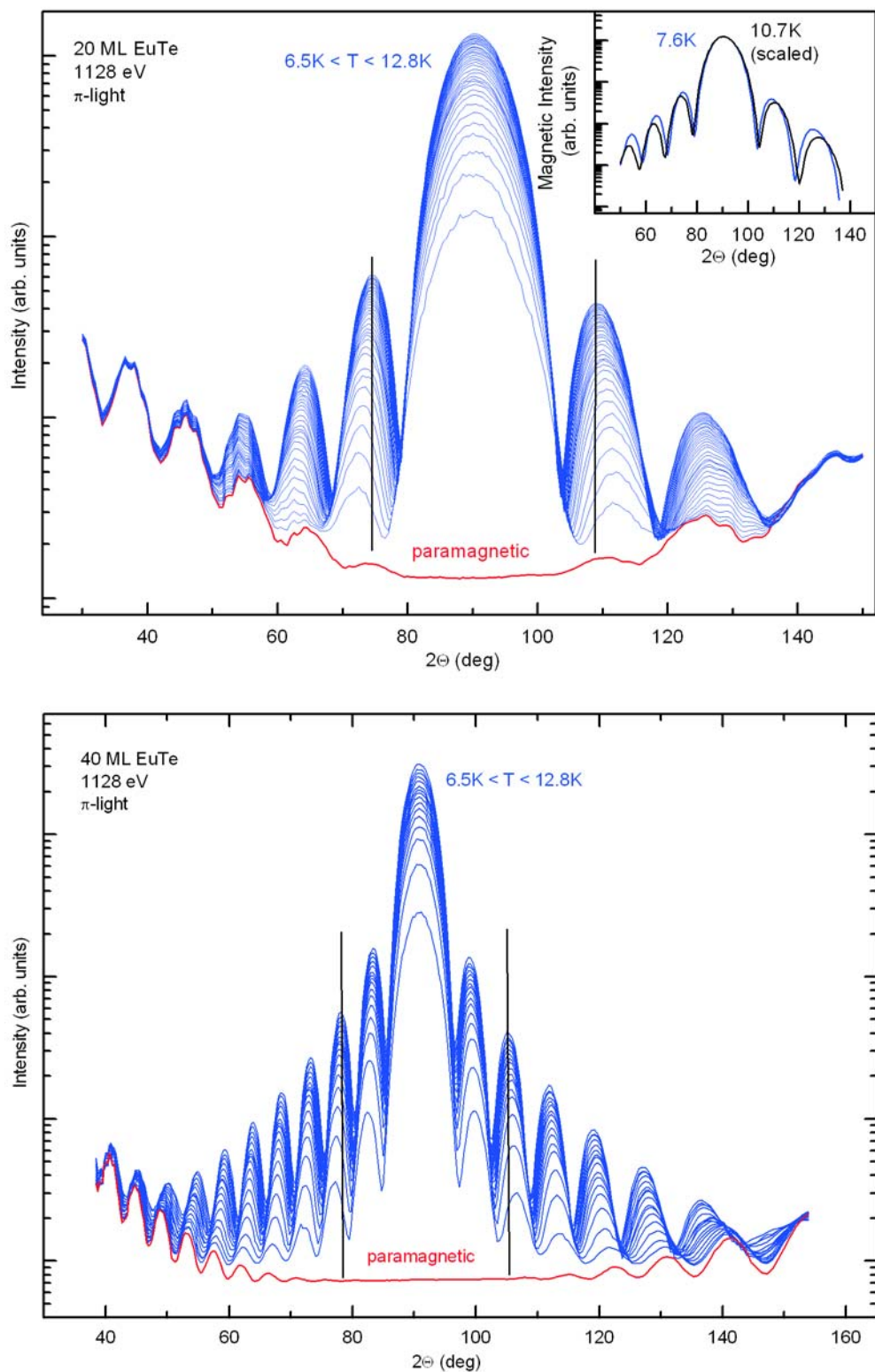
Figure 7.15: *Magnetic Laue patterns from the 20-ML and 40-ML EuTe samples as a function of temperature.*
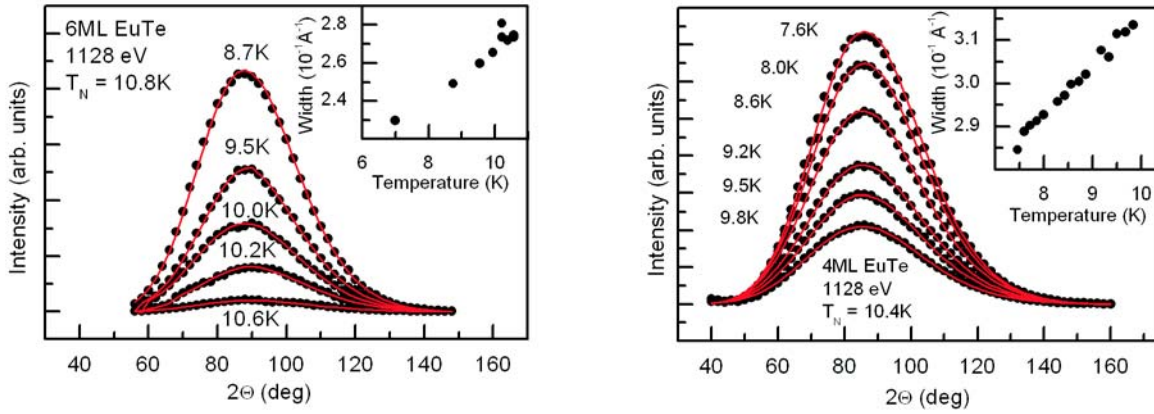
Figure 7.16: *Normalized magnetic signal from the 4-ML and 6-ML thin EuTe samples measured at various temperatures. The red lines correspond to Gaussian fits. The obtained peak widths are given in the insets.*

7.2.1 Qualitative Discussion

The magnetic Laue patterns of the 20-ML and 40-ML sample are characterized by a shift of the Laue minima and side maxima away from the principal reflections. Analogous behavior is observed for the thinner EuTe films as shown for the 6-ML and 4-ML sample in Fig. 7.16. In these cases, the principal reflection is the only observable signal and the only effect of temperature is a broadening of the principal Bragg reflection with increasing temperature, which can be analyzed for all studied EuTe films. Figure 7.17 displays the change of the peak widths between the lowest temperature reached and $0.95T_N$ in terms of the change of the corresponding magnetic thicknesses, given by the inverse peak widths. This property, which is a measure of the average loss of magnetic layers, is found to be independent of sample thickness within the error bars for samples thicker than 13 ML. Hence, the reason for this behavior must be the same for all samples, it is the presence of two surfaces. The change is rather small and corresponds on an average loss of 1.5 ML. For the thinner samples ($N < 14$ ML), the average number of lost magnetic layers decreases with thickness. This is expected, considering the limit of only two layers, both surface layers, where no peak-broadening can occur.

    Interestingly, already the 6-ML sample shows a reduced broadening, while the 14-ML sample does not. This means that between 3 ML and 7 ML are influenced by the surfaces. Following Binder and Hohenberg [56], this observation suggests the presence of a magnetization profile characterized by a reduced absolute magnetization $m(j)$ in a region of up to 7 ML close to the surface. Accordingly, the 20-ML sample has an optimum thickness for a more quantitative analysis, with ≈ 6 central layers hardly influenced by the surface up to $0.95T_N$. Following these considerations, the Laue patterns of the 20-ML sample were recorded with a very high density of points and in steps of 0.1 K over the entire accessible temperature range of the ordered phase. The next section describes the analysis of these 64 magnetic Laue patterns.

7.2.2 Reconstruction of Magnetization Profiles

The challenge in the following data analysis is to quantify the layer-dependent magnetizations, $m(j)$, of the various layers j, from the measured Laue patterns. This goal is impeded by the general limitation of a diffraction experiment: While the scattered amplitude $A(Q)$ contains all information necessary for a unique reconstruction of the real-space structure, it is the intensity $I(Q) \propto |A(Q)|^2$ that is
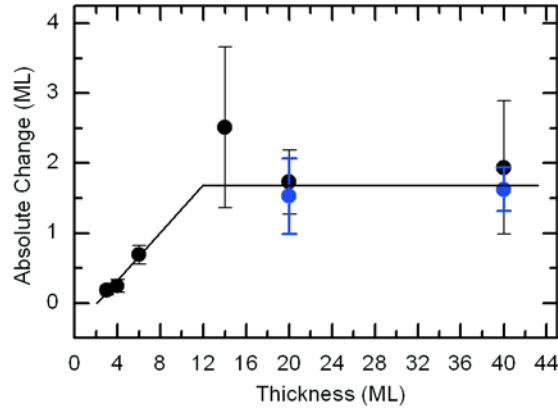
Figure 7.17: *Average loss of magnetic layers obtained from the difference of the inverse peak width at low temperatures and $0.95 T_N$ as a function of sample thickness. The black dots are determined by Gaussian fits to the principal maxima of the Laue patterns, while the blue dots correspond to the shift of the side minima in the case of the thicker films.*

recorded. The measuring process destroys the phase information and a unique real-space reconstruction is therefore not possible from the measured intensity alone. Precisely, the Laue patterns contain only information on the auto-correlation function of the real-space structure. This is the well-known phase-problem in diffraction. The situation is further complicated by the fact that even the auto-correlation function is not precisely known as a consequence of data scatter and the limited range of accessible reciprocal space.

However, the reconstruction of the magnetization profiles in the present analysis can rely on several known facts regarding the real-space magnetization and a few reasonable assumptions. First, the overall magnetic structure is known to be a simple AFM modulation normal to the surface. Second, the magnetic scattering densities are not smoothly varying, but are strongly localized at the Eu^{2+} lattice sites. These strongly localized scattering centers will provide the spatial sensitivity to achieve atomic-layer-resolved magnetization profiles. Furthermore, the analysis does not rely on a single Laue pattern. The search is rather for an initial smooth structure that changes monotonically with temperature in such a way that all measured Laue patterns are simultaneously fitted.

For this purpose, highly developed and consequently complex least-squares-fitting algorithms are not suited, they minimize the deviation of a theoretical model from a dataset by changing the fit parameter along the direction of maximum gradient in parameter space. Such a method is highly efficient as long as the number of local minima in parameter space is rather small. In the case of an ambiguous problem and a large number of local optima these algorithms are characterized by a large probability to get trapped in local minima in parameter space. The simulated annealing method, introduced by Kirkpatrick et al. in 1983, optimizes a set of parameters to match a specified set of conditions, avoiding local minima. It is the tool of choice for ambiguous problems and was applied, e.g. , to estimate the ground-state energy of spin glasses (see appendix B).

The following analysis utilizes the concept of simulated annealing, which is introduced together with the applied algorithm in appendix B. The measured intensities from the 20-ML sample as a function of temperature are shown in Fig. 7.15. The pure magnetic contributions are separated by subtracting the paramagnetic background signal. The resulting magnetic intensities $I_{T,meas.}(2\Theta)$ are described by the one-dimensional lattice sum (see appendix A):
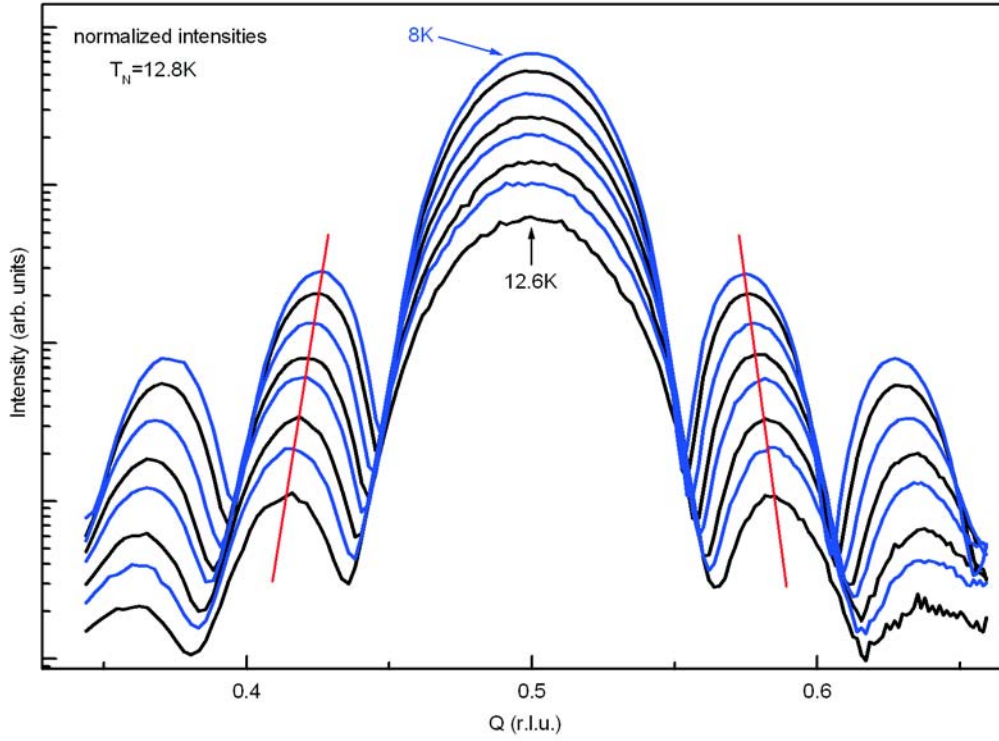
Figure 7.18: *Normalized magnetic signals from the 20-ML film. These symmetric Laue patterns essentially represent the pure reciprocal space dependence of the scattered intensity.*

$$I_{T,meas.}(2\Theta) \propto I_{0,T} \left| \sum_{j=0}^{N-1} (-1)^j m(j,T) e^{iQ_z jd} e^{-\frac{jd\mu}{\sin\omega}} \right|^2 \quad , \tag{7.12}$$

where N denotes the number of layers with a layer spacing d, and $I_{0,T}$ denotes the intensity of the incident beam. In addition, the geometry dependences as discussed in appendix A have to be taken into account. The aim of the analysis is to reconstruct the layer- and temperature-dependent magnetizations $m(j,T)$. The magnetic data were normalized with respect to the incident intensity, the angular-dependent absorption in the EuTe film and PbTe cap-layer, the polarization dependence, and the angular dependence caused by the integration over the detector acceptance (appendix A), to yield the pure Q-dependence of the magnetic Laue patterns (Fig. 7.18).

Instead of the Laue patterns, the corresponding Fourier transforms were analyzed that represent the auto-correlation function of the real-space magnetization distribution. In the case of a perfect AFM structure consisting of N layers, this function exhibits (2N-1) extreme values of alternating sign spaced by the lattice constant, with a triangular envelope function[7] symmetrically centered at zero. Figure 7.19(a) shows the real part of the Fourier transform[8] of the magnetic Laue pattern measured at 7.2 K. As expected, essentially 39 alternating extrema are observed. The absolute values of these extrema are plotted as a function of the layer index in 7.19(b). The triangular shape is not perfect due to the limited Q-range. However, the temperature-dependent changes of the Laue patterns are

---

[7]This is the auto-correlation of a perfect rectangle that represents the finite film thickness.
[8]The Fourier transform was restricted to the Q regime of high data quality shown in Fig. 7.18.
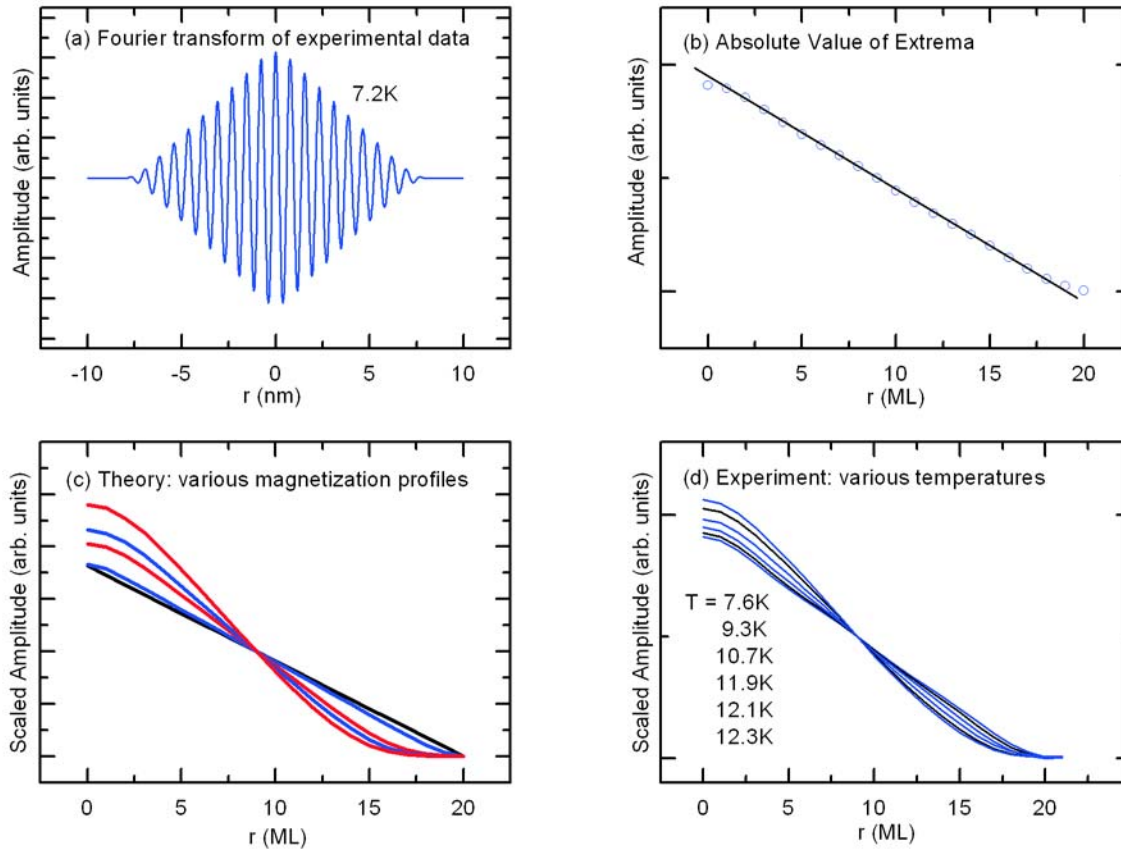
Figure 7.19: *(a) Fourier transform of a measured magnetic Laue pattern. (b) Absolute values of the extrema of (a) plotted versus layer index. (c) Calculated extrema of auto-correlation functions for various magnetization profiles characterized by a decreased surface magnetization. (d) Extrema of Fourier transforms of experimental Laue patterns for various temperatures.*

also reflected in the evolution of the extremal values as shown in Fig. 7.19(d). For comparison, (c) displays theoretically calculated auto-correlation functions that correspond to magnetization profiles of increasingly reduced magnetization in the near-surface layers.

This shows that the information on the magnetization profiles obtainable from the Laue patterns is essentially contained in these 20 extreme values of the corresponding Fourier transforms. It is therefore convenient to deal with these quantities rather than the Laue patterns, which reduces the computational effort.

The analysis was carried out in two steps. In the first step, 22 free parameters $s(j, T)$, describing the amplitudes scattered by the individual layers (scattering strength) were used, restricted only to change sign from layer to layer. 22 layers were used to account for intermixing at the interfaces (chapters 5.2.1, 7.1.1, 7.1.4). Simultaneously for all 64 temperatures, the 22 parameters were determined to reproduce the experimental auto-correlation function. In the analysis, the temperature-dependent scattering strength of each layer was forced to decrease monotonically with temperature.

Figure 7.20 displays the resulting real-space scattering-strength profiles. These profiles are characterized by an essentially constant value for the inner layers and a reduced scattering strength for layers at the two interfaces. Superimposed are oscillations and a systematic smooth decrease from left
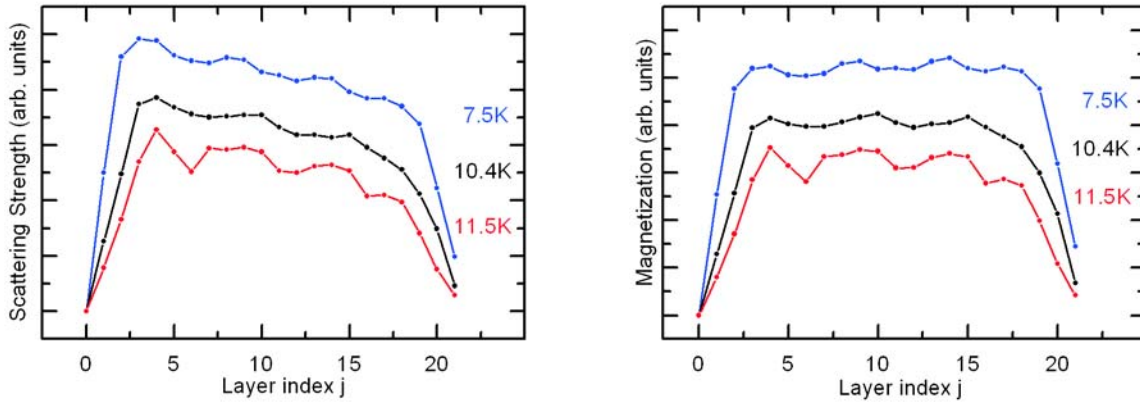
Figure 7.20: *Left: Scattering-strength profile of a 20-ML EuTe film obtained from an optimization with 22 free parameters for three different temperatures. Right: Layer-dependent magnetization resulting from the scattering-strength profile after correction for photon absorption.*
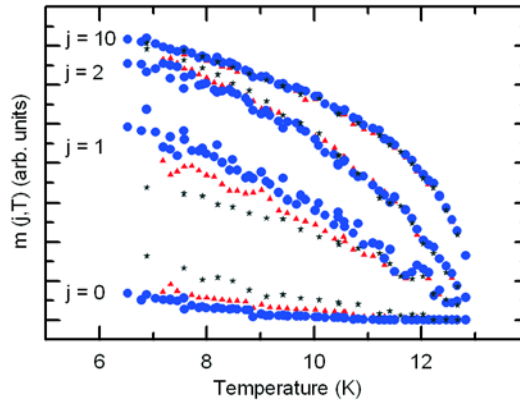

Figure 7.21: *Temperature dependence of the individual-layer magnetizations of the 20-ML EuTe film. j labels the 22 layers. Different colors correspond to analysis runs with different starting parameters.*

to the right. The systematic smooth decrease across the film is due to photon absorption. Correction with a factor $e^{j\mu}$ yields symmetric profiles for $\mu = \frac{1}{80}$, corresponding to an attenuation length of 80 ML, in nice agreement with the results of chapter 7.1.2. The symmetric magnetization profiles in the right panel of Fig. 7.20 essentially reflect the behavior predicted by Binder and Hohenberg: The magnetization at the interface is reduced with respect to the central layers and this reduction increases with increasing temperature. In addition, the number of affected layers increases towards T_N.

The analysis with essentially freely varied $s(j, T)$ provides a general picture. However, details like the oscillatory behavior are unphysical and lead to jumps in the temperature dependence. Therefore, the shape of the magnetization profile is further restricted in the second step of the analysis to yield a more reasonable description. To this end, the scattering-strength profile is described by a simple function that takes the results of the first step of the analysis into account. The layer-dependent scattering-strength is given by layer-dependent magnetizations $m(j)$ multiplied by an exponential function to account for absorption. The magnetization profile is assumed to be symmetric, modeled by the function:
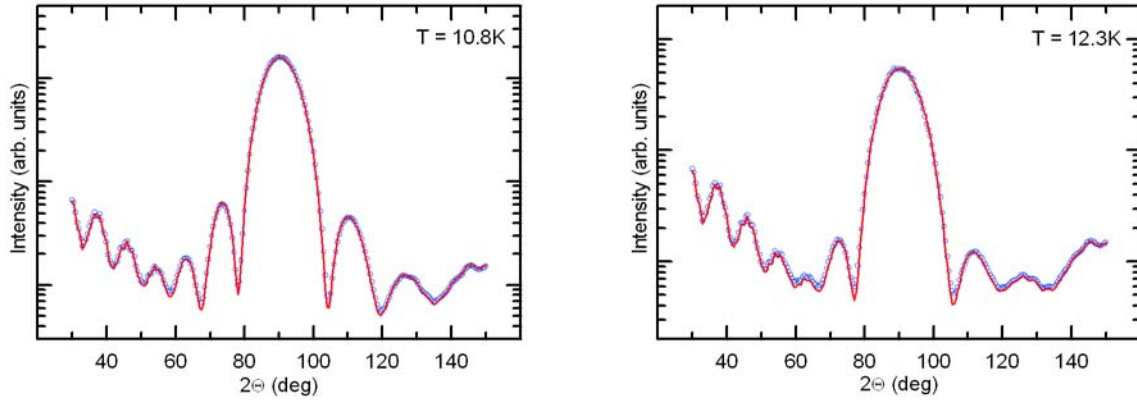
Figure 7.22: *Laue patterns calculated from the derived magnetization profiles for the 20-ML sample (red lines), in comparison with the raw data (blue dots).*

$$
\begin{aligned}
|m(j)| &= & m_b & \quad, |10.5 - j| \leq N_b \\
&= & m_b(1 - R \cdot |10.5 - N_b - j|^{\alpha}) & \quad, |10.5 - j| > N_b \ \text{and} j \neq 0, 1, 20, 21 \\
&= & m_b \cdot m_{EP}(1 - R \cdot |10.5 - N_b - j|^{\alpha}) & \quad, j = 1, 20 \\
&= & m_b \cdot m_{PE} \cdot m(1) & \quad, j = 0, 21
\end{aligned}
$$

with a constant inner magnetization and a power law describing the decrease of the magnetization towards the surfaces. Two additional free parameters allow larger deviations of the magnetization of the outermost two layers to account for unfilled layers. The entire profile scales with the magnetization of the center of the sample, m_b. The effective scattering strength then reads $s(j) = (-1)^j \, m(j) \, e^{-j\mu}$. The free parameters N_b, m_b, R, α, m_{EP}, m_{PE}, and μ were determined utilizing the optimization scheme discussed above. The final result is given by the temperature-dependent layer-resolved magnetizations $m(j, T)$ shown in Fig. 7.21. The analysis was tested for various starting parameters and cooling rates within the simulated annealing scheme (appendix B), the respective results are given by the different colors. The excellent agreement of the results of the different analysis runs demonstrates the stability of this procedure. Only the outermost two layers exhibit a comparably large variation due to the very small scattering contribution of these layers to the entire signal. Figure 7.22 displays Laue patterns calculated from the final magnetization profiles according to Eq. 7.12 (red lines). Comparison with the experimental data (blue dots) demonstrates the excellent quantitative data description.
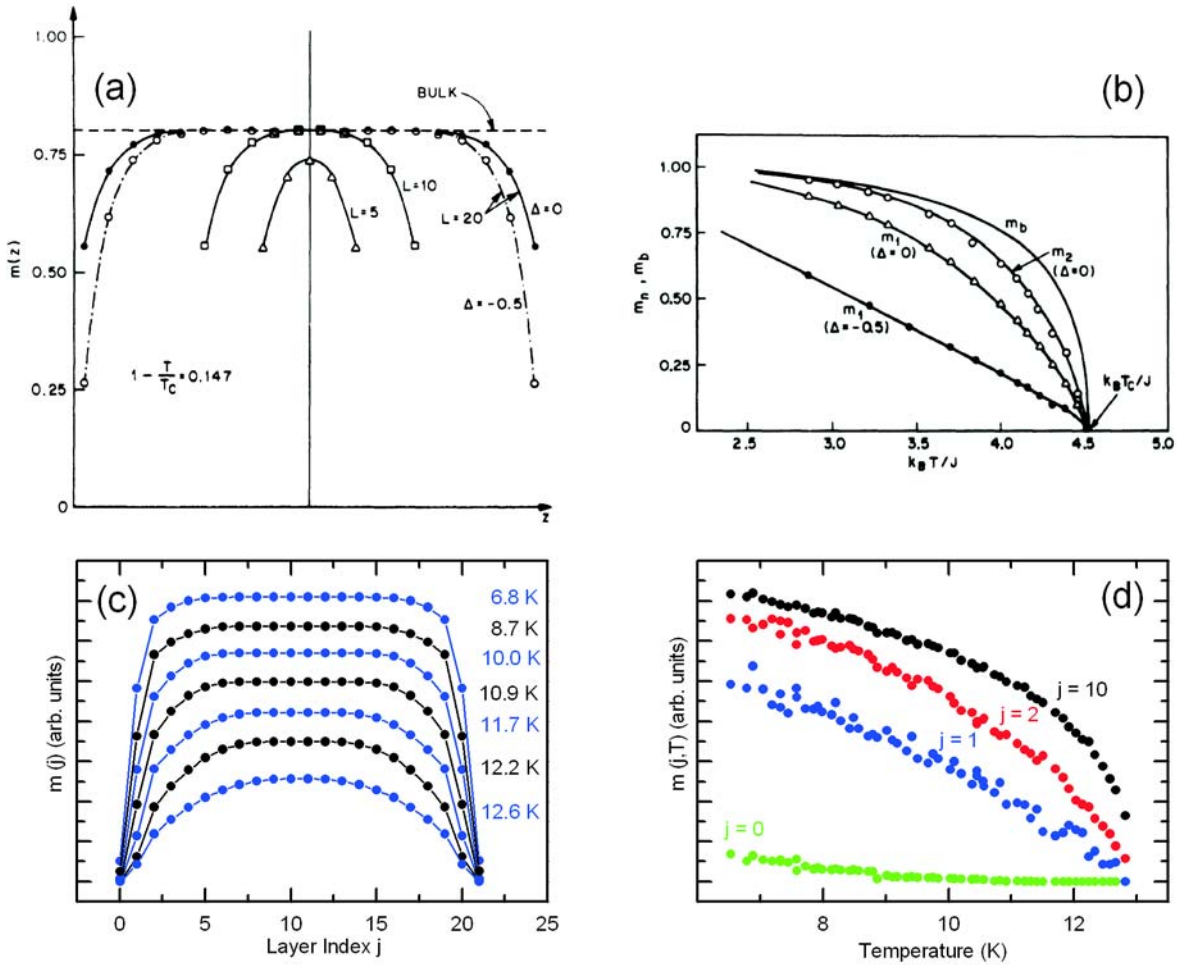
Figure 7.23: *(a) Magnetization profiles according to Binder and Hohenberg [56]. (b) Corresponding temperature dependences of the layer magnetizations. (c) Experimental magnetization profiles of the 20-ML film. (d) Temperature dependences of the individual-layer magnetizations.*

### 7.2.3   Atomic-Layer-Resolved Magnetization Profiles

The analysis described in the previous section yields the temperature-dependent layer-resolved magnetizations of the AFM EuTe film, corroborating the results of a more than thirty-years-old calculation [56]. Although these theoretical predictions were partly confirmed by some experiments, an entire atomic-layer resolved magnetization profile was not reported yet. A comparison of both, the theoretical calculations and the present results is shown in Fig. 7.23, revealing an excellent general agreement. Even at the lowest temperature, the magnetization across the film is not constant, but deviates from the center in the four outermost layers at each interface, particularly in the two layers closest to the interface ($j = 0, 1$). With increasing temperature, this deviation of the magnetization of the outermost layers does not only increase, but also the range of reduced magnetization extends into the film. At $T = 0.95T_N$, the number of layers characterized by a reduced magnetization reaches a value of about seven, in perfect agreement with the expectations from the initial qualitative inspection of the thickness-dependent behavior of the peak width (cf. section 7.2.1). Close to the ordering temperature, the entire sample is affected and no central layers with constant magnetization can be found
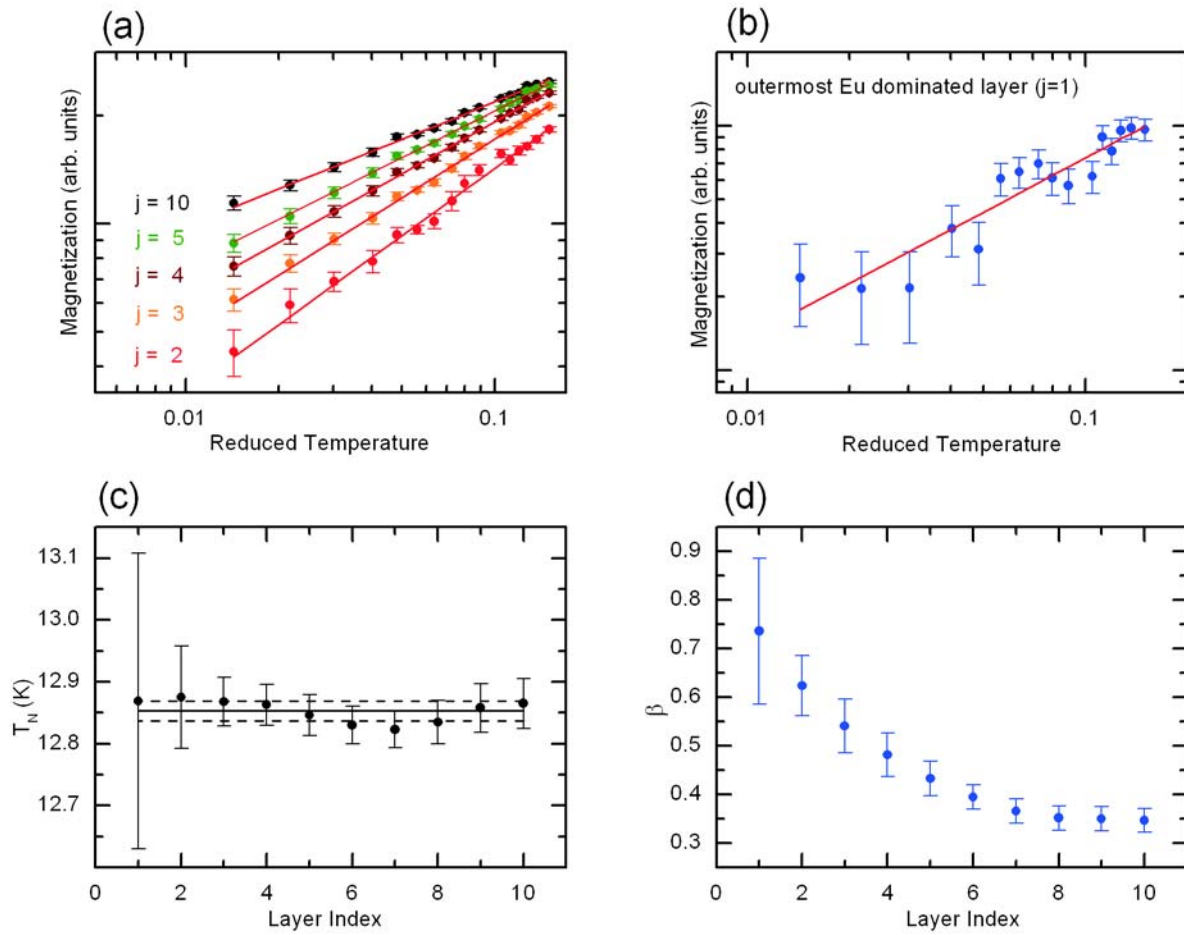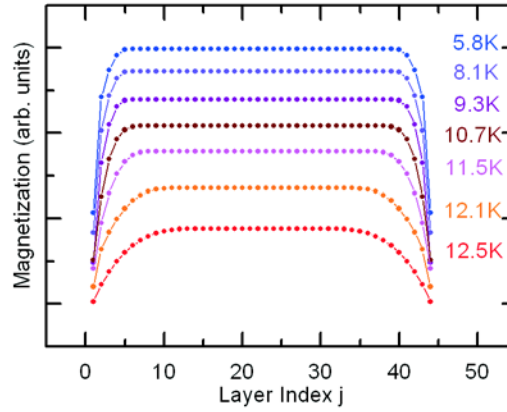
Figure 7.24: *Power-law description of the temperature dependence of the individual-layer magnetizations. (a) and (b): Layer magnetizations on a reduced temperature scale. The reduced temperature refers to an ordering temperature as marked by the solid line in (c). The red lines display linear fits on the double logarithmic scale. (c) Ordering temperatures obtained from independent power-law descriptions of the individual-layer magnetizations. (d) Exponents β resulting from (a) and (b). The error bars are determined by fits with different ordering temperatures within the range indicated by the broken lines in (c).*

anymore. This expansion of the region of reduced magnetization from the interface towards the film center clearly demonstrates different temperature dependences for the individual-layer magnetizations as shown in 7.23(d) for the three outermost layers ($j = 0, 1, 2$) and a center layer ($j = 10$). Obviously, the outer layers are characterized by a significantly faster decrease of the magnetization with increasing temperature. These findings perfectly meet the expectations from the results of Binder and Hohenberg [56], namely reduced magnetizations characterized by a faster decrease with temperature for the layers close to the interface (Fig. 7.23(a),(b)).

The temperature-dependent layer magnetizations can be analyzed in terms of a critical phase transition. The ordering temperatures of the individual layers, shown in Fig. 7.24 (c), which result from power-law descriptions of the individual-layer magnetizations, are essentially equal within rather small error bars. The uncertainties of the individual $m(j, T)$ close to T_N prevent a precise study of the critical behavior and in particular do not allow a precise determination of critical exponents. However,
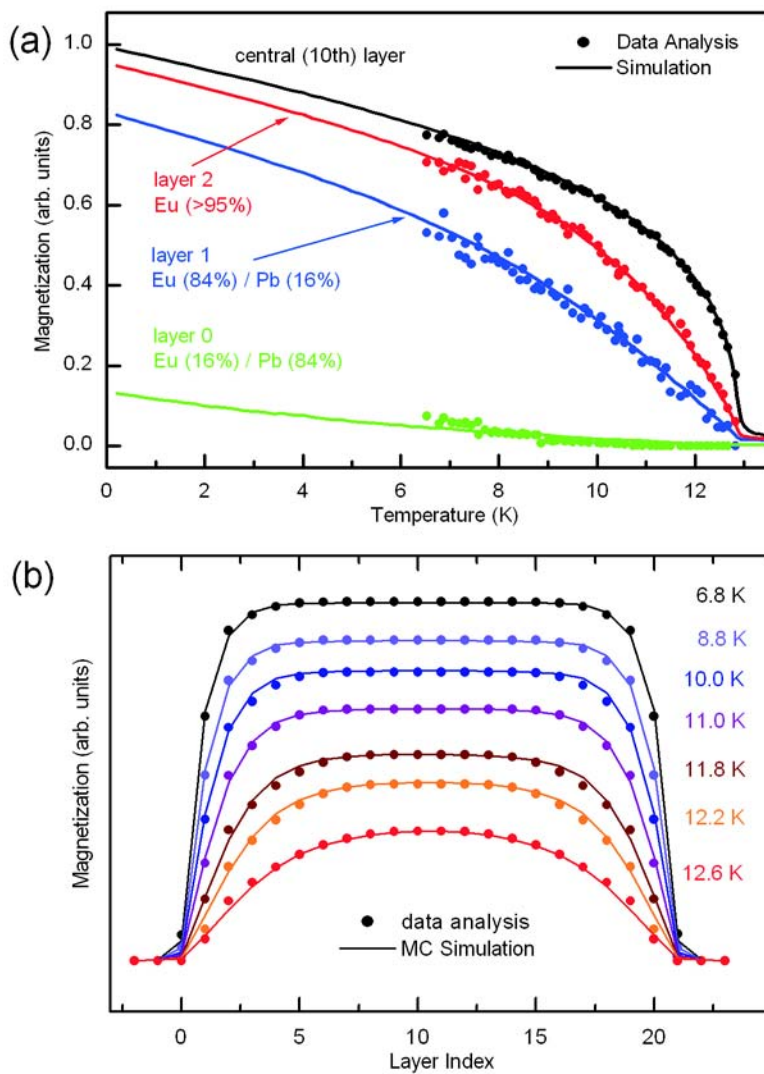
Figure 7.25: *Magnetizations (dots) derived from the Laue patterns of the 20-ML EuTe film compared to the realistic MC simulations (solid lines) described in the text. (a) Temperature dependence. (b) Layer dependence.*

Figure 7.26: *Magnetization profiles of the 40-ML EuTe sample derived by analysis of the Laue patterns.*

the exponents β versus layer index (Fig. 7.24(d)), obtained from the power-law description shown in (a) and (b), exhibit a clear tendency from $\beta = (0.35 \pm 0.03)$ consistent with the 3D-Heisenberg, 3D-XY, and 3D-Ising model towards significantly larger values of up to $\beta = (0.74 \pm 0.15)$ for $j = 1$, in excellent qualitative agreement with the predictions discussed in chapter 1.3.2. The strongly reduced magnetizations of the outermost layers cannot be attributed to a pure surface effect, since even for $T \rightarrow 0$, the magnetization of the central layers is not reached. This points to an additional reduction of the magnetization due to the intermixing between EuTe and PbTe at the interface.

These results have triggered detailed calculations for thin EuTe films. To extend the comparison with theory to a more quantitative level and to understand the influence of the chemical profile, Monte-Carlo (MC)-simulations were carried out by W. Söllinger from the University of Linz. These simulations followed essentially the original treatment of Binder and Hohenberg, but realistic coupling constants were applied. To account for the changes in the inter-atomic distances induced by the epitaxial strain, the nn exchange J_1 is split into two separate components $J_{1,p}$ and $J_{1,s}$ within and across neighboring Eu (111) lattice planes, respectively. With the values of $J_{1,p}/k_B = 0.223$ K, $J_{1,s}/k_B = 0.185$ K and $J_2/k_B = -0.324$ K, the experimentally observed ordering temperature is exactly reproduced. The model also permits to take imperfect interfaces into account by reducing the average number of neighboring Eu atoms at the interface. For a consistent description of all experimental $m(j, T)$ data, Eu occupancies of the interface layers 0 to 2 of 16%, 84%, and 96%, respectively, were required. Taking this chemical interface profile into account, the calculations (solid lines in Fig. 7.25) reproduce all details of the experimental results and provide a detailed quantitative understanding of the temperature-dependent magnetization profile in the thin EuTe film. The obtained chemical profile identifies layer $j = 0$ as essentially the outermost Pb layer, containing only a few Eu ions due to interdiffusion or surface steps as expected from the growth mode of EuTe on PbTe discussed in chapter 5.2. Also layer 1 is substantially affected by the intermixing, while layer 3 is almost a perfect EuTe layer.

The results of this analysis reflect a general behavior of EuTe films as can be seen from the magnetization profiles derived for the 40-ML sample shown in Fig. 7.26. The behavior of the 40-ML sample near the surface is almost identical to that found for the 20-ML film. However, as a consequence of the dominant contribution of the film center to the entire magnetic signal, the results from the 40-ML film are characterized by larger uncertainties. Nevertheless, this second example clearly demonstrates the observed behavior to be a pure surface effect that occurs independent of the thickness of the sample,

underlining the general character of the present results. To my best knowledge, no comparable result was reported so far and the findings from this prototypical Heisenberg system are in perfect qualitative agreement with earlier theory and with realistic simulations in a quantitative way.

The observed behavior indicates an ordinary second-order phase transition at the ordering temperature T_N. At the critical point, the magnetic order vanishes in all layers and only short-range magnetic correlations remain. These magnetic correlations induce an extremely weak magnetic scattering signal. The almost negligible charge scattering background at the position of the AFM reflection, however, permits a study of those correlations over a wide range of temperature, which is the subject of the following section.

7.3   Magnetic Short-Range Correlations and Dimensional Crossover

The microscopic interactions between the Eu spins create the ordered magnetic structure discussed in the previous section once the temperature is low enough, i.e. when the energy gain due to long-range magnetic order exceeds the thermal energy. No stable spin configuration can be found above this temperature regime. Both phases are separated by the critical point ($T = T_N, H = 0$), where the phase transition from the AFM to the paramagnetic regime occurs. But also above T_N, neighboring spins tend to align as a consequence of the still present interaction. The dominant thermal energy prevents stable spin arrangements even on the local scale, but within a certain volume, the directions of the spins will still be correlated. These short-range magnetic correlations cause diffraction signals that differ from the flat background noise of uncorrelated moments. This phenomenon is called magnetic critical scattering. Due to the typically small dimension of the volume of correlated spins, quantified by the correlation length ξ, the related scattering signal is much broader than that of the long-range ordered structure below T_N. The quality of such weak magnetic scattering data is strongly limited by the noise originating from any underlying charge scattering contribution, which often restricts critical scattering experiments to a small temperature region in the vicinity of T_N. In the present experiment, the almost negligible charge scattering background leads to useful magnetic scattering signals up to temperatures as high as $1.5 \cdot T_N$. This large temperature interval above T_N permits to follow the behavior of short-range magnetic correlations down to microscopic distances.

One interesting aspect is the change in critical behavior caused by the finite thickness of the sample. A dimensional crossover is expected to occur as a function of sample thickness and temperature (see chapter 1.3.1). In particular, the thickness dependence is well known from numerous experiments [39, 47–49]. A dimensional crossover is typically inferred from the distinct change of one of the critical exponents in the power laws given in table 1.1. While these simple power laws usually provide a quantitatively sufficient description of experimental data over a large temperature interval, several corrections can become necessary at higher temperatures. Theoretically, the thermodynamic quantities are described by series expansions, where the simple power law is the leading contribution, e.g. for the susceptibility χ:

$$\chi \approx \chi_0 t^{-\gamma}(1 + a_1 t^y + ...) \quad , \tag{7.13}$$

with a universal exponent $y > 0$ [140]. The influence of anisotropies or long-range interactions, like the dipole-dipole interaction, can cause further temperature-dependent deviations from the isotropic towards a modified critical behavior that reflects the additional restrictions [141, 142]. These will alter the critical exponents as observed experimentally [143]. It is for these reasons, that the experimental situation concerning the question of universality classes of magnetic phase transitions often is vague even in the case of seemingly simple systems. A pure dimensional crossover is directly
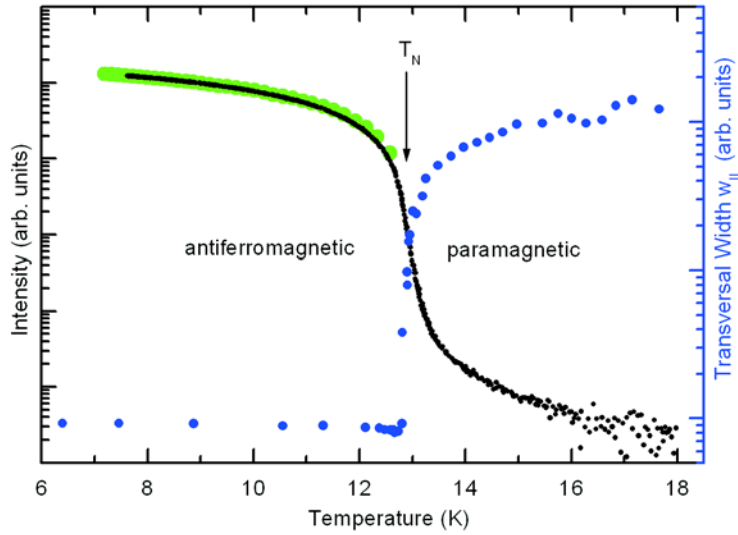
Figure 7.27: *Temperature dependence of the magnetic intensity and peak width across the phase transition obtained from the 20-ML sample. Green dots: Integrated intensity in the ordered phase. Black dots: Intensity measured at the position of the AFM reflection. Blue dots: Transversal width.*

related to the truncation of the divergence of the correlation length ξ. Therefore, this quantity should allow for a rather straightforward interpretation of dimensional crossover effects.

Scattering experiments provide access to ξ, since they measure the Fourier transform of the spatial two-spin correlation function $G(r)$ as discussed in chapter 1.2. With the classical Ornstein-Zernike form (Eq. 1.13), the intensity distribution associated with the critical fluctuations is essentially described by a Lorentzian [29], with the half width at half maximum (HWHM) equal to ξ^{-1}. In the case of magnetic phase transitions, the commonly applied method is magnetic neutron diffraction, as performed, e.g. , on EuO and EuS by Als-Nielsen et al. [27, 30], but also resonant magnetic x-ray diffraction was applied. One of the first experiments that utilized x rays to record magnetic critical scattering, was performed by Thurston et al., who studied the helical antiferromagnet Ho at the L_3 resonance in the hard x-ray regime [144]. However, the study of dimensional crossover effects requires experiments on thin and ultra-thin samples, where the magnetic signal in both, neutron and hard x-ray experiments is too weak. Resonant magnetic soft x-ray scattering turned out to be the tool of choice in this case. One of the first studies utilizing soft x rays to monitor the critical behavior was performed by Ott et al. on thin films of holmium [54], finding a crossover to two-dimensional behavior between 11 ML and 16 ML of Ho.

7.3.1 Magnetic Critical Scattering from EuTe

In the present experiment, magnetic short-range correlations were studied by $\Theta/2\Theta$ and rocking scans at the peak position of the AFM reflection $\mathbf{Q}_{AFM}$. The former scan mode probes the correlations along the surface normal direction, the latter reflects the in-plane behavior. While the rocking scans are almost free of charge scattering background, the longitudinal data display the sum of the magnetically scattered photons and the charge reflectivity. Therefore, the background signal recorded at 30 K ($\approx 3 \cdot T_N$) was subtracted.

Figure 7.27 summarizes characteristics of the 20-ML sample. The large drop of the intensity at T_N (black and green dots) is accompanied by a sudden huge increase of the transversal width $w_\parallel$
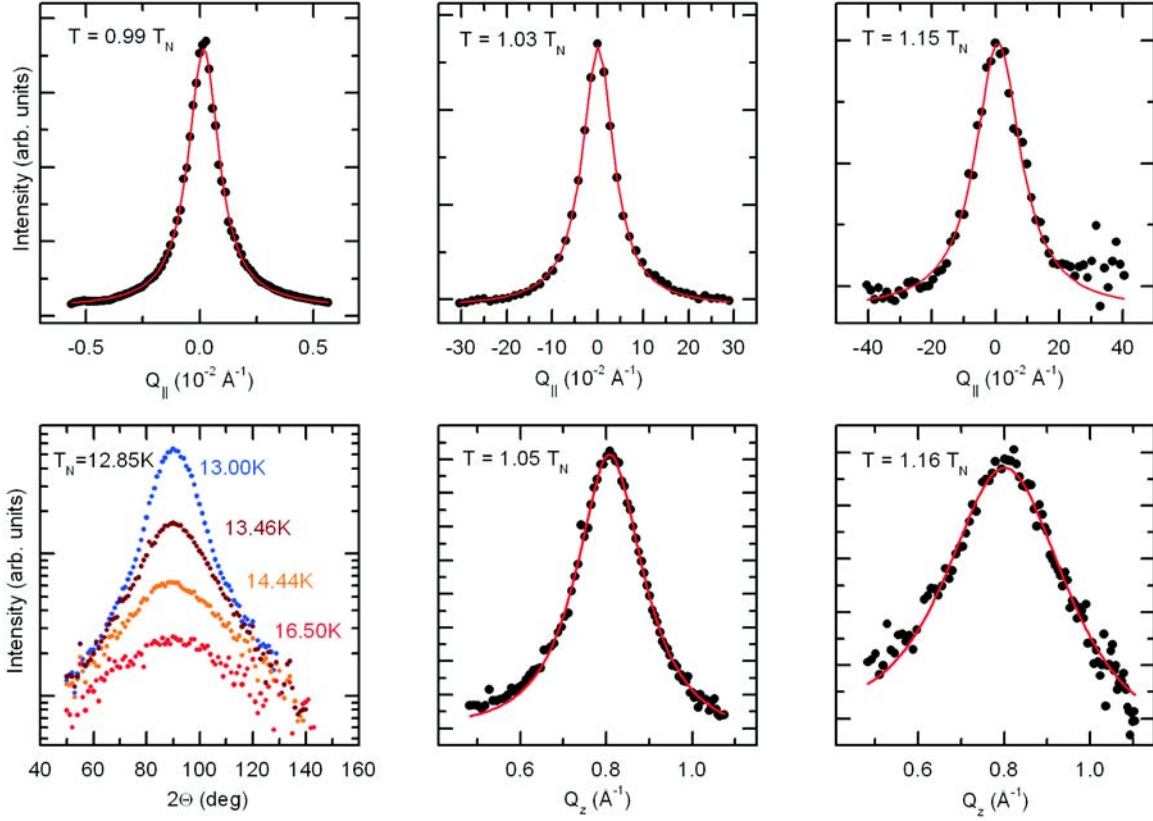
Figure 7.28: *Critical scattering signals from 20 ML of EuTe. Top: Rocking scans, recorded at the maximum of magnetic intensity, characterized by a strong broadening in the paramagnetic phase (center, right) with respect to the narrow distribution in the ordered phase (left). Note the different $Q_{||}$ scales. Bottom: Longitudinal scans for various temperatures above $T_N = 12.85\,K$, corrected for geometry-dependent influences as described in appendix A. Red lines represent fits as described in the text.*

(blue dots). These temperature-dependent intensities and peak widths yield information on the critical behavior of the sample. The integrated intensity (green dots) represents the order parameter and is usually used to determine the critical exponent β. However, the peak intensity recorded at $\mathbf{Q}_{AFM}$ (black dots) is different. This difference is caused by the longitudinal peak broadening due to the layer dependence of the magnetization, as discussed in the previous chapter. Hence, a power law description of the integrated intensity only characterizes the average sample behavior and can cause misleading interpretations in terms of universality classes. Instead, the individual-layer magnetizations have to be analyzed, as discussed in the previous section.

Unlike the peak intensity, the pronounced increase of the peak width above T_N provides a far more direct view on the critical behavior. While these widths can be obtained in good approximation by Lorentzian fits to the data, a precise analysis has to take the angular-dependent influences of the photon absorption in the PbTe cap layer, the polarization factor as well as the integration over the detector acceptance into account. Therefore, the data, corrected for the geometry dependences as described in appendix A, were analyzed using the relation:

$$I(\omega, 2\Theta) \propto \int_{det} I_{CS}(\mathbf{Q}')d\Omega \quad , \tag{7.14}$$
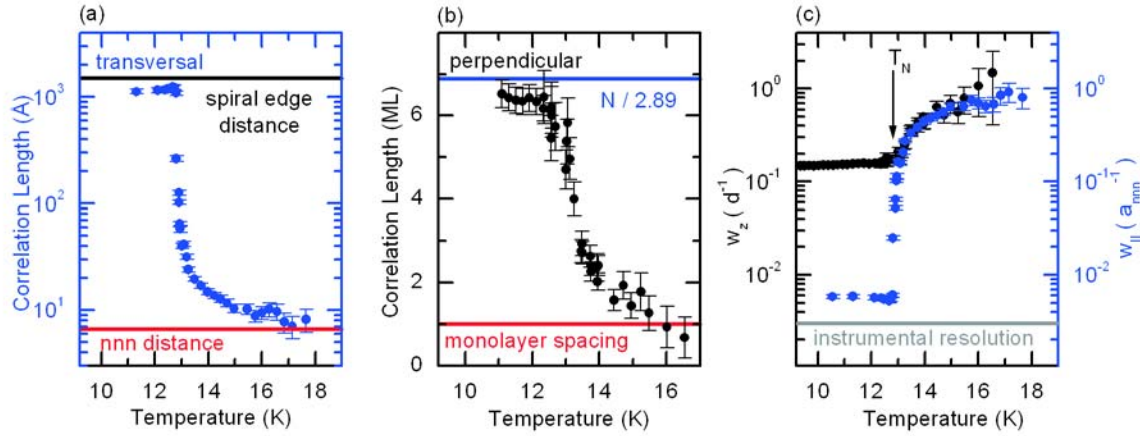
Figure 7.29: *(a): In-plane correlation length. The red and the black line represent the nnn spacing and the mean distance of the spiral edges at the surface of the EuTe samples, respectively. (b) Correlation length along the perpendicular direction. The red line corresponds to the monolayer spacing while the blue line marks about one third of the sample thickness. (c) Corresponding transversal (blue dots) and longitudinal (black dots) peak widths normalized with respect to the inverse of the nnn spacing and the monolayer spacing, respectively. The gray line gives the instrumental resolution.*

where $\mathbf{Q}'(\omega, 2\Theta)$ denotes the deviation of the scattering vector from $\mathbf{Q}_{AFM}$. The integral considers the detector acceptance. The Fourier transform of the correlation function can be approximated by a Lorentzian [145] :

$$I_{CS}(\mathbf{Q}') \propto \frac{\chi}{1 + \frac{\left|\mathbf{Q}'_{||}\right|^2}{w_{||}^2} + \frac{|Q'_z|^2}{w_z^2}} \quad , \tag{7.15}$$

which accounts for different widths along the in-plane ($w_{||}$) and perpendicular (w_z) direction and leads to an excellent description of all measured data as shown in Fig. 7.28. From the temperature dependence of $w_{||}$ and w_z and the intensities, the ordering temperature can be determined with high accuracy to permit a discussion in terms of a reduced temperature t.

7.3.2   Temperature-dependent Correlation Length

Not only the transversal width increases at the critical point but also the longitudinal width w_z. The increase of w_z is less pronounced, since the minimum width is limited by the thickness of the films. Figure 7.29 displays the transversal (a) and longitudinal (b) magnetic correlation lengths, covering the entire range of relevant length scales. The observed transversal correlation lengths are not limited by the instrumental resolution[9] as shown in Fig. 7.29 (c) and range from the mean distances of the structural spiral edge surface features of about 150 nm, discussed in chapter 5.2.1, down to the next nearest neighbor spacing a_{nnn}, i.e. a range larger than two orders of magnitude is probed from macroscopic structural dimensions down to the minimum microscopic distances. The longitudinal width is limited by the sample thickness. The divergence of the correlation length along this direction is indeed truncated at about one third of the film thickness as predicted (see chapter 1.2.) and has been observed for

---

[9]The instrumental resolution is calculated from the horizontal detector acceptance and the divergence of the incident x-ray beam.
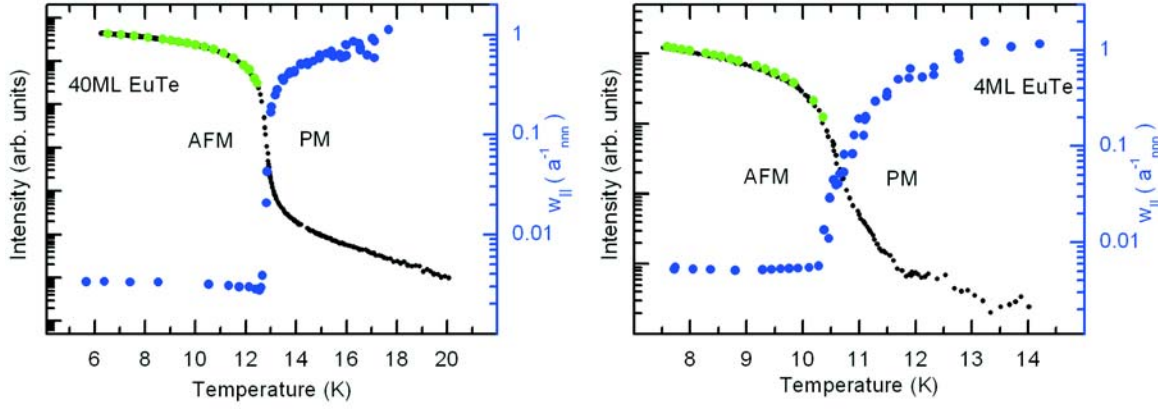
Figure 7.30: *Temperature dependences of intensities and peak widths obtained from 40 ML and 4 ML of EuTe. Green dots: Integrated magnetic intensity in the ordered phase. Black dots: Intensity measured at the position of the AFM reflection. Blue dots: Transversal width.*

structural phase transitions by Nickel et al. [53], but so far not for magnetic phase transitions. Towards higher temperatures, the experiment could follow the decrease of the perpendicular correlations down to the monolayer spacing.

These detailed data allow for a comparison of the longitudinal and transversal behavior. In general, the evolution of the correlation length along different directions depends on the corresponding coupling mechanisms and the microscopic structure. Therefore, the amplitudes describing the power-law like divergence of the correlation length are non-universal quantities. However, from the isotropic Hamiltonian (see chapter 2.2) that describes EuTe, one would expect an essentially isotropic behavior of the correlation length, and the associated peak width should only depend on the temperature and the relevant microscopic distances. Figure 7.29 (c) displays the observed longitudinal and transversal peak widths normalized with respect to the relevant microscopic distances given by the monolayer spacing d in the case of the longitudinal intensity distributions, and the nnn spacing $a_{nnn} = 6.59\,\text{Å}$ for the transversal data. The essentially identical temperature dependences and magnitudes of both widths above the ordering temperature reveal the essentially isotropic nature of the correlation length and demonstrates that both properties are governed by the same critical exponent ν.

7.3.3   Dimensional Crossover

The growth of the critical fluctuations in thin samples is restricted along the surface normal direction by the sample thickness, as found in the 20-ML EuTe film. It is therefore interesting to extend this study to thinner films, where that influence of spatial limitation should increase. This is readily achieved, as demonstrated in Fig. 7.30.

The thickness dependence of the in-plane growth of the volumes of correlated spins is shown in Fig. 7.31 by the temperature dependence of $w_\parallel$ on a reduced temperature scale. While the thickest samples (40 ML, 20 ML, and 14 ML) behave identical, thinner films (7 ML, 6 ML, 4 ML) show a clear deviation. This deviation occurs in a temperature region of $0 < t < 0.1$, where ξ is truncated by the finite film thickness, and disappears at higher t, where the correlation length is substantially decreased. The deviation is most striking in the 3-ML sample. There, in contrast to all other samples, the increase of $w_\parallel$ with t is much slower. The exceptional behavior of the 3-ML sample is also reflected in the longitudinal behavior shown in Fig. 7.32. Above T_N, all thicker films show an in-
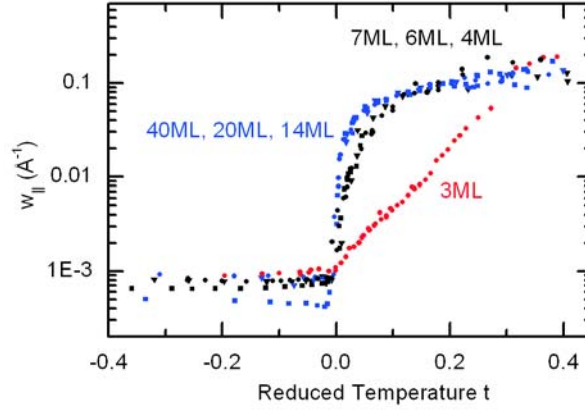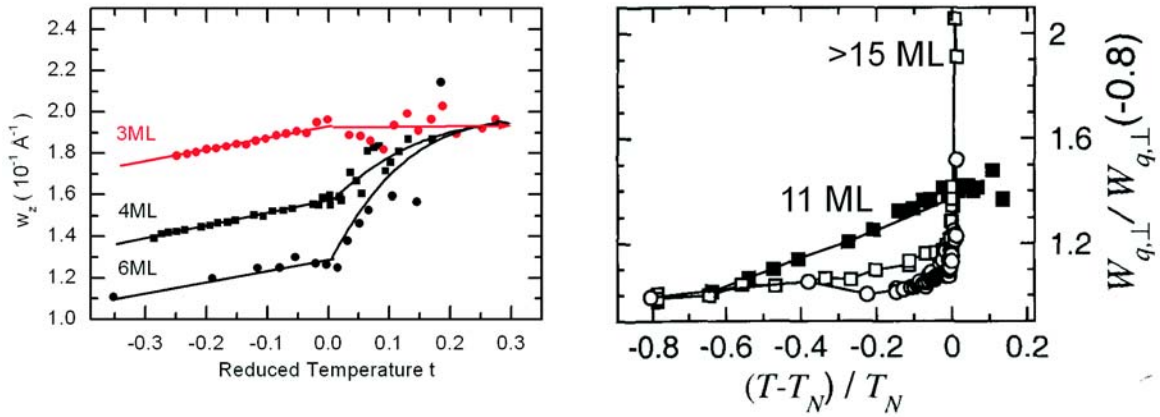
Figure 7.31: *Temperature dependences of the transversal widths $w_{||}$ of various EuTe samples on a logarithmic scale. Blue symbols: Samples with an almost unchanged ordering temperature (40 ML, 20 ML, 14 ML). Black symbols: 4 ML, 6 ML, and 7 ML, characterized by a slightly reduced ordering temperature. Red dots: 3 ML of EuTe.*

creasing longitudinal width. The longitudinal width of the 3-ML film, on the other hand, has reached the maximum value at the ordering temperature and stays constant in the temperature regime above. Hence, the observed smooth decrease of $w_{||}$ towards T_N with decreasing T, belongs to a pure in-plane growth of the critical fluctuation. One could argue that the exceptional behavior of the 3-ML sample is caused by the chemical roughness [146]. However, the same argument would hold for the 4-ML sample, which shows essentially unchanged critical behavior. Therefore, this change of the growth of the critical fluctuations that occurs between 4 ML and 3 ML, must be attributed to a dimensional crossover effect.

It is instructive to compare these findings with those of holmium metal [54]. The direct comparison given in Fig. 7.32 and Fig. 7.33 clearly reveals that both AFM systems exhibit the same behavior. Like EuTe, thicker holmium films show an abruptly increasing longitudinal and transversal width above T_N. The 11-ML holmium film, on the other hand, exhibits the same smooth increase of $w_{||}$ and the constant longitudinal width above T_N as 3 ML EuTe. This comparison of the results of both studies demonstrates that the observed changes in the transversal behavior and the constant longitudinal width above T_N are related. Interestingly, the strong changes in both systems occur at a film thickness of the order of the magnetic period length. In the case of the holmium films, this finding was attributed to a temperature-dependent crossover from three-dimensional to two-dimensional XY-behavior in terms of a Kosterlitz-Thouless transition [147], which predicts a behavior of the width according to:

$$w \propto w_0 \ e^{-bt_{KT}^{-1/2}} \tag{7.16}$$

where t_{KT} denotes the reduced temperature with respect to the characteristic Kosterlitz-Thouless temperature T_{KT} of the system and $b \approx 1.5$ is a constant parameter. This scenario clearly can be ruled out from the totally straight increase of $w_{||}$ of the 3-ML sample on the simple logarithmic scale of Fig. 7.31 over the entire large range of t. Instead, a simple exponential relation $w \propto e^{b'T}$ has to be concluded, which cannot be described in terms of a Kosterlitz-Thouless transition. However, the distinct change from a power-law like divergence of the in-plane correlation length towards exponential behavior at constant perpendicular correlation length, observed in both systems, strongly indicates

Figure 7.32: *Left: Thickness dependence of the temperature-dependent longitudinal peak width w_z in thin EuTe films. Black dots: 6 ML. Black squares: 4 ML. Red dots: 3 ML. Lines are guides to the eyes. Right: Analogous behavior observed for three thin Ho films [54].*
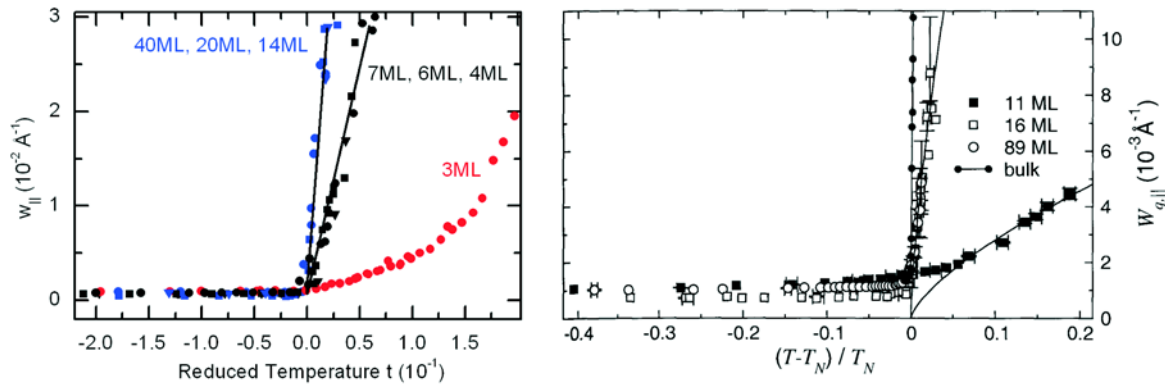
Figure 7.33: *Left: Thickness dependence of the temperature-dependent transversal peak width $w_{||}$ in thin EuTe films. Blue squares: 40 ML. Blue dots: 20 ML. Blue triangles: 14 ML. Black triangles: 7 ML. Black squares: 6 ML. Black dots: 4 ML. Red dots: 3 ML. The solid lines are guide to the eyes. Right: Temperature-dependent transversal width obtained from three thin holmium films [54].*
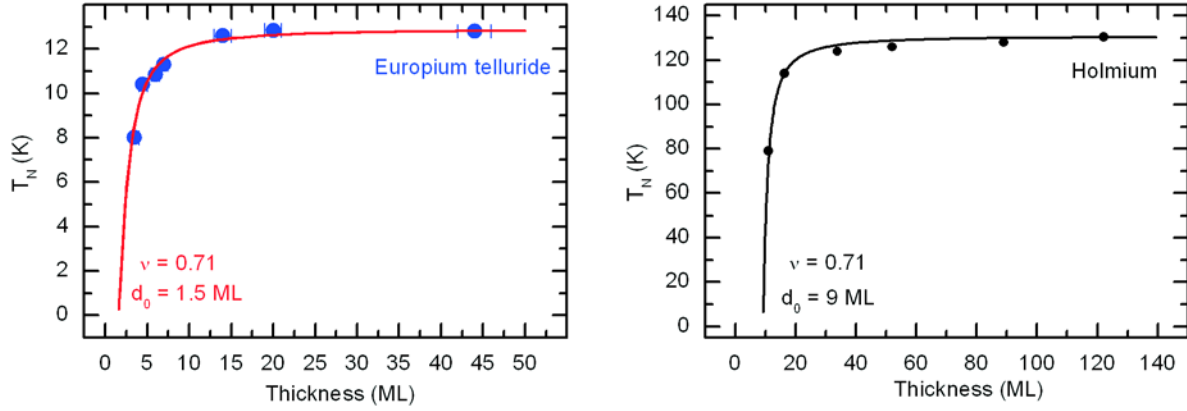
Figure 7.34: *Left: Thickness-dependent ordering temperature of the studied thin EuTe films. The line represent a fit according to Eq. 1.16. Right: Dependence of T_N on the film thickness of the long-period AFM holmium structure for comparison.*

a dimensional crossover at a thickness that scales with the AFM period length. This result closely resembles the thickness dependence of the ordering temperature, which in the case of Ho also shows a relation to the magnetic period length as discussed in chapter 6.

The ordering temperatures of almost all EuTe samples are well above the EuTe bulk ordering temperature of 9.8 K as displayed in Fig. 7.34. This is caused by the epitaxial strain as discussed in chapter 7.2.3. Therefore, the finite-size effect in the strained film has to be analyzed with respect to this enhanced ordering temperature. While the ordering temperature of 14 ML of EuTe is only slightly reduced compared to 40 ML, already 16 ML of Ho are characterized by an ordering temperature of less than 90% of the bulk value. The first EuTe sample, that shows a discernable decrease of T_N is the 7-ML thin film, and even for 4 ML, T_N is still quite high. It is only the 3-ML EuTe sample that shows a reduction of T_N, which is comparable to that of 11 ML of Ho. The thickness dependence of T_N of the short-period antiferromagnet EuTe is similar to that of the long-period antiferromagnet Ho and can be described by Eq. 1.16, if an offset thickness $d_0 = 1.5$ ML is assumed. This comparison shows that dimensional crossover and finite-size effect of the ordering temperature in long-period magnetic structures are related to the length of that period.

An open question remains concerning the exponential behavior of $w_\parallel$ in the quasi-2D case. In both materials the drastic change of the in-plane behavior occurs exactly in the thickness regime, where the ordering temperature becomes extremely sensitive to small changes of the film thickness. Therefore local changes of the film thickness may strongly influence the growth of critical fluctuations. And indeed, EuTe is characterized by an interface roughness of at least one layer, as discussed in connection with structural properties (see chapter 7.1.1, see also chapter 5.2.1). This will also hold for the Ho sample, embedded between Y layers [54]. These rough interfaces with a local variation of the thickness in a sensitive thickness regime (3 ML in the case of EuTe and 11 ML in the case of Ho) might prevent the isotropic growth of the critical fluctuations and lead to an exponential behavior. However, at present this is quite speculative and will require a detailed theoretical analysis.